Seasonal radiative modeling of Titan's stratospheric temperatures at low latitudes

Bruno Bézard[a*], Sandrine Vinatier[a], Richard K. Achterberg[b]

[a]: LESIA, Observatoire de Paris, PSL Research University, CNRS, Sorbonne Universités, UPMC Univ. Paris 6, Université Paris-Diderot, Sorbonne Paris Cité, 5 place Jules Janssen, 92195 Meudon, France

[b]: University of Maryland, Department of Astronomy, College Park, MD 20742, United States

[*] Corresponding author.
E-mail address: bruno.bezard@obspm.fr

Contact details: Bruno Bézard
LESIA, Bât. 18
Observatoire de Paris, section de Meudon
92195 Meudon cedex
France

Phone: (33) 1 45 07 77 17
Fax: (33) 1 45 07 28 06

Published in Icarus, Volume 302, 1 March 2018, Pages 437–450
https://doi.org/10.1016/j.icarus.2017.11.034

ABSTRACT

We have developed a seasonal radiative-dynamical model of Titan's stratosphere to investigate the temporal variation of temperatures in the 0.2-4 mbar range observed by the Cassini/CIRS spectrometer. The model incorporates gas and aerosol vertical profiles derived from Cassini/CIRS and Huygens/DISR data to calculate the radiative heating and cooling rate profiles as a function of time and latitude. At 20°S in 2007, the heating rate is larger than the cooling rate at all altitudes, and more specifically by 20-35% in the 0.1-5 mbar range. A new calculation of the radiative relaxation time as a function of pressure level is presented, leading to time constants significantly lower than previous estimates. At 6°N around spring equinox, the radiative equilibrium profile is warmer than the observed one at all levels. Adding adiabatic cooling in the energy equation, with a vertical upward velocity profile approximately constant in pressure coordinates below the 0.02-mbar level (corresponding to 0.03-0.05 cm s^{-1} at 1 mbar), allows us to reproduce the observed profile quite well. The velocity profile above the ~0.5-mbar level is however affected by uncertainties in the haze density profile. The model shows that the change in insolation due to Saturn's orbital eccentricity is large enough to explain the observed 4-K decrease in equatorial temperatures around 1 mbar between 2009 and 2016. At 30°N and S, the radiative model predicts seasonal variations of temperature much larger than observed. A seasonal modulation of adiabatic cooling/heating is needed to reproduce the temperature variations observed from 2005 to 2016 between 0.2 and 4 mbar. At 1 mbar, the derived vertical velocities vary in the range -0.05 (winter solstice) to 0.16 (summer solstice) cm s^{-1} at 30°S, -0.01 (winter solstice) to 0.14 (summer solstice) cm s^{-1} at 30°N, and 0.03-0.07 cm s^{-1} at the equator.

Key words: Titan, atmosphere; Atmospheres, structure; Atmospheres, dynamics

1. Introduction

Due to Saturn's obliquity of 26.7°, Titan experiences large seasonal variations of insolation. The 0.056 eccentricity of Saturn's orbit adds a significant modulation to this insolation. Above the 10-mbar level, Titan's radiative time constant is less than a Titan year (29.5 Earth years) (Strobel et al. 2009, Flasar et al. 2014) so that significant seasonal variations of temperature are expected in the mid-stratosphere and mesosphere.

Infrared observations by the IRIS instrument aboard the Voyager 1 spacecraft in November 1980 pointed out a north-to-south asymmetry of temperatures in the 0.4-1 mbar region, with temperatures at 55°S being higher than at 55°N by 4 and 8 K at 1 and 0.4 mbar respectively (Flasar et al. 1990). These observations occurred shortly after northern spring equinox, at a heliocentric longitude $L_s \approx 9°$. Flasar and Conrath (1990) proposed that the asymmetry was due to a phase lag in the response of the atmosphere to the seasonally-varying insolation due to dynamical inertia. On the other hand, Bézard et al. (1995) suggested that the asymmetry results from the larger concentrations of infrared radiators (photochemical gases and aerosols) present at high northern latitudes.

The Cassini Composite Infrared Spectrometer (CIRS) aboard Cassini allowed us to monitor the thermal structure of Titan's stratosphere from July 2004 to September 2017, which corresponds to $L_s \approx 293°$. Combining limb- and nadir-viewing observations between 2004 and 2006, Achterberg et al. (2008a) retrieved the temperature field over the pressure range 5×10^{-3}-5 mbar from about 75°S to 75°N. The corresponding season was around northern mid-winter (L_s = 293-323°). Compared with Voyager 1 observations, the north-to-south asymmetry was stronger and temperatures at 55°S were higher than at 55°N by about 18 and 11 K at 1 and 0.4 mbar respectively. Compared to southern latitudes, high northern latitudes were then experiencing reduced solar heating and enhanced abundances of photochemical gases and aerosols, both of which likely contribute to the lower temperatures. Besides this asymmetry, mid-stratosphere temperatures on Titan were reaching their maximum at latitudes 0-30°S. On the other hand, the stratopause was found higher and warmer beyond 50°N than anywhere else on the satellite, which very likely results from adiabatic heating from downwelling air at winter polar latitudes. Achterberg et al. (2011) extended the analysis of Achterberg et al. (2008a) using Cassini/CIRS data up to December 2009, i.e. shortly after northern spring equinox ($L_s \approx 4°$). Between 2004 and 2009, a large decrease of temperatures in the stratopause region (above the 0.1-mbar level) was found beyond 30°N. Elsewhere in the stratosphere and lower mesosphere, the temperature variations did not exceed 5 K.

The temporal and latitudinal variations of temperature observed in the stratosphere and lower mesosphere result from combined variations of the insolation, modulating the solar heating rate, of the atmospheric composition, which governs the radiative cooling and solar heating rates, and of dynamical motions, which provide adiabatic heating and cooling. To try to assess the relative importance of these actors, it is first necessary to constrain as precisely as possible the radiative forcing terms, which requires a good knowledge of the distribution of the radiatively-active gases and aerosols. Such information is available from Cassini/CIRS, which measures in nadir- and limb-viewing geometry the thermal emission spectrum of Titan from 10 to 1495 cm^{-1}. This allows the retrieval of the gas concentration and aerosol extinction profiles that contribute to the radiative cooling between approximately 130 and 450 km (5-0.005 mbar) (e.g. Vinatier et al. 2010a, 2010b, 2015). The Descent Imager/Spectral Radiometer (DISR) aboard the Huygens probe measured the optical properties and vertical distribution of haze particles between 0 and ≈150 km (Tomasko et al. 2008c, Doose et al. 2016) on 14 January 2005 near 10°S. Used with a correct representation of the methane opacity, these results allow us to compute the solar heating rate profile as a function of zenith angle. Combining Huygens/DISR and Cassini/CIRS data, Tomasko et al. (2008b) were able to investigate the heat balance at the location and time of the Huygens descent. They inferred that the day-averaged solar heating rate profile exceeded the cooling rate profile by a maximum of 0.5 K/Titan day (0.03 K/Earth day) near 120 km altitude (5.5 mbar) and concluded that the general circulation must redistribute this heat to higher latitudes.

In Titan's stratosphere, a meridional circulation, similar to Hadley cells on Earth, is driven by the latitude-dependent solar heating (see a review of Titan's general circulation in Lebonnois et al. 2014). General Circulation Models (GCMs) have been developed to investigate Titan's dynamics, in particular the superrotation characterized by prograde zonal winds up to ~200 m s^{-1} in the winter stratosphere (see Newman et al. 2011, Lebonnois et al. 2012 and Lora et al. 2015 for recent three-dimensional GCMs). These models show a pole-to-pole circulation, particularly in the stratosphere, with rising motion in the summer hemisphere and subsidence in the winter hemisphere except around equinox, when a more symmetric equator-to-pole circulation takes place throughout the atmosphere. They generally succeed in reproducing at least qualitatively the dominant features of Titan's atmospheric structure, such as the zonal wind pattern and temperature field, but suffer from approximations in the treatment of the radiative transfer and/or various other simplifications. The strong subsidence at high winter latitudes predicted by the GCMs is confirmed by the high temperatures and the large enrichment in minor photochemical species observed in the upper stratosphere and mesosphere (Achterberg et al. 2011; Teanby et al. 2007, 2009; Vinatier et al. 2007, 2010a). The temperature anomalies observed in winter around the north pole have been used to estimate downward vertical velocities of ~10 cm s^{-1} around 0.01 mbar in 2005-2007 (Achterberg et al. 2011). Changes in the vertical abundance profiles of minor species observed near the south pole in autumn were also used to derive the following vertical velocities: from 0.1 to 0.4 cm s^{-1} near 0.003 mbar in 2010-2011 and 2011-2012 (Teanby et al. 2012, Vinatier et al. 2015), 0.25 cm s^{-1} near 0.01 mbar in 2011-2012, and 0.4 cm s^{-1} near 0.02 mbar in 2015 (Vinatier et al. 2017a).

The goal of this paper is to investigate the heat balance of Titan's stratosphere using a seasonal radiative model based on measurements by Cassini/CIRS of the distributions of the radiative agents and state-of-the-art representation of gas and aerosol spectral properties. We also take into account constraints from Huygens/DISR measurements. We then calculate the season-dependent radiative solution for the temperature profile and compare it with the observed variations of temperature at different levels and latitudes to derive constraints on the dynamical heating/cooling. Here, we restrain our analysis to mid-latitudes (30°S-30°N) where gas and aerosol do not exhibit large seasonal variations. Section 2 describes the temperature data, retrieved from Cassini/CIRS measurements, with which we are comparing our model. Section 3 presents our seasonal radiative model and the gas and aerosol distributions used in the radiative transfer code to calculate heating and cooling rates. Radiative model results are presented in Section 4 and compared with observations to constrain the missing adiabatic heating and cooling terms. Also shown is a calculation of the radiative time constant as a function of pressure level. We discuss these results in Section 5 and present our conclusions in Section 6.

2. Observations

Retrievals of Titan's temperature field are routinely achieved using nadir and limb observations of the ν_4 band of methane through Focal Plane FP4 of Cassini/CIRS. This focal plane covers the interval 1050-1495 cm^{-1} at a spectral resolution adjustable from 15.5 to 0.5

cm^{-1} (apodized). It consists of a 10-pixel linear array, with a 0.27-mrad field of view (FOV) per pixel (Flasar et al. 2004). Temperature maps were retrieved by Achterberg et al. (2008a) for mid-winter conditions (2004-2006) combining nadir-viewing (2.8-cm^{-1} resolution) and limb-viewing (15.5-cm^{-1} resolution) sequences. The nadir data cover latitudes from 90°S to 60°N and yield information in a pressure range of about 5-0.2 mbar while the limb data cover latitudes from 75°S to 85°N and yield information in a pressure range ≈ 1-0.005 mbar. Achterberg et al. (2011) extended the analysis to cover 5.5 years of Cassini/CIRS observations from July 2004 to December 2009, just after northern spring equinox. Here we use a further extended data set encompassing observations up to June 2016, i.e. Titan flybys T0 to T118 (Achterberg et al. in preparation). For each flyby, zonal-mean temperatures were obtained by zonally averaging temperatures retrieved from individual nadir-viewing spectra (2.8-cm^{-1} resolution) using 5° latitude bins with 2.5° spacing and interpolating the retrieved temperatures onto a uniform latitude grid for each flyby. Averaging was done in a reference frame that removes the 4° offset of the stratospheric symmetry axis from the surface pole (Achterberg et al. 2008b). In our analysis, we used temperatures retrieved at 0.2, 0.5, 1, 2 and 4 mbar, which cover the range of maximum temperature information. Note that these temperatures actually represent a vertical average over 1 to 1.5 scale heights due to the width of the contribution functions in the methane band and the filtering applied in the retrieval process. We restrained our analysis to equatorial and mid-latitudes and selected data at $\theta = 0°$, 30°N and 30°S. For a given latitude θ and a given flyby, we averaged the three temperatures retrieved by Achterberg et al. (in preparation) at latitudes θ-2.5°, θ and θ+2.5°. Figure 1 shows the retrieved 1-mbar temperatures as a function of time for these three latitudes. The error bars correspond to the standard deviation (SD) of temperatures in each 5° bin divided by square of root of the number of data points. Seasonal variations are clearly visible in this data set. At the equator, the 1-mbar (~185 km) temperature increases slightly from 2005 to 2011-

2012 (by less than 1 K), and decreases more noticeably after 2012 (by ~4 K between 2012 and 2016). At 30°N, the temperature increases by ~4 K from 2005 to 2012 and decreases by about the same amount from 2012 to 2016, while at 30°S the temperature regularly decreases by ~8 K from 2005 to 2016.

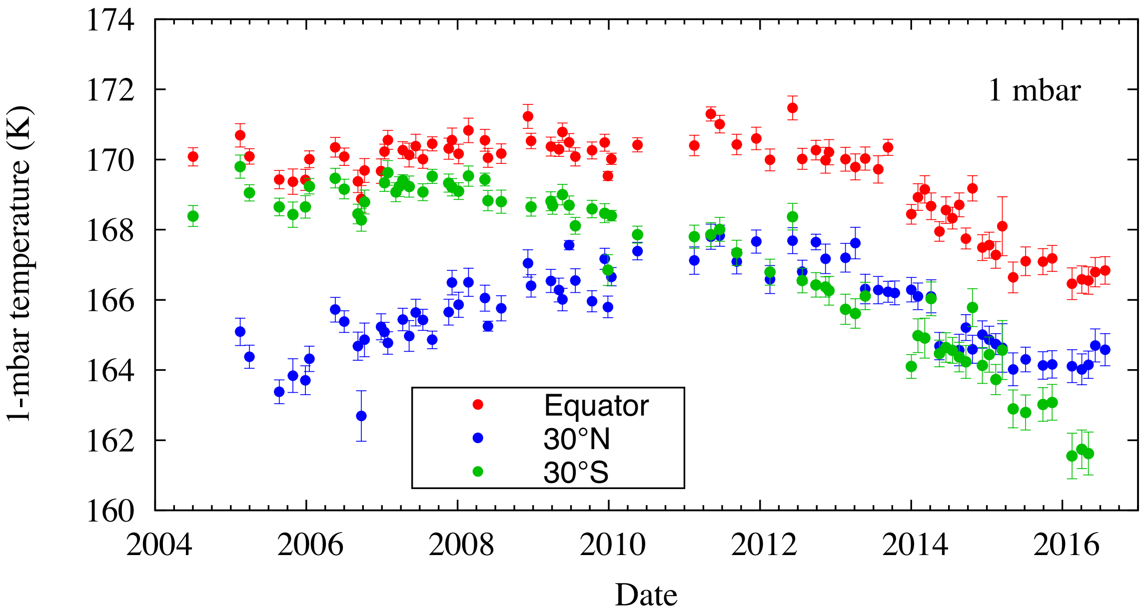

Figure 1: Time variation of 1-mbar temperatures retrieved from Cassini/CIRS measurements at three latitudes, 0°, 30°N and 30°S.

Vinatier et al. (2015) produced maps of temperature and composition from selected sequences of CIRS limb spectra recorded between October 2006 and May 2013 at a resolution of either 0.5 or 15.5 cm^{-1}. Reliable information extends from 5 to 0.001 mbar, a region below which the temperature profile smoothly joins the Huygens/HASI profile measured *in situ* at 10°S in January 2005 (Fulchignoni et al. 2005). We used Vinatier et al.'s results around 6°N, a latitude least sensitive to seasonal effects, as a reference profile to test our model and investigate the heat balance at this latitude. To smooth out small local temperature variations, we averaged four temperature profiles recorded at 4-5°N, on January 2007 (Ls = 327°), December 2009 (Ls = 4°), June 2010 (Ls = 11°) and May 2011 (Ls = 21°), thus corresponding to northern mid-winter to mid-spring conditions. This profile is shown in Fig. 7. The 1-SD formal error bar due to noise propagation is about ± 0.2 K in the range 0.1-1 mbar increasing to ± 0.3 K at 0.01 mbar and ±0.4 K at 5 mbar. The standard deviation of our set of four temperature profiles is larger, 0.5 to 1.5 K from 0.2 to 2 mbar, 2 K at 0.1 and 5 mbar and 5 K at 0.01 mbar.

3. Seasonal radiative model

We developed a one-dimensional seasonal radiative-dynamical model to investigate the observed temperature variations in Titan's stratosphere. We solve for the energy equation:

$$\frac{\partial T(z)}{\partial t} = h(z) - c(z) - w(z)\left(\frac{g(z)}{C_p} + \frac{\partial T(z)}{\partial z}\right). \tag{1}$$

$h(z)$ is the solar heating rate equal to $-\frac{g}{C_p}\frac{dF_*(p)}{dp}$, where F_* is the downward solar flux, $c(z)$ is the radiative cooling rate equal to $-\frac{g}{C_p}\frac{dF_{IR}(p)}{dp}$ with F_{IR} being the upward thermal emission flux, w the upward vertical velocity, C_p the specific heat, and g the acceleration of gravity. The term $w(z)\frac{g(z)}{C_p}$ represents the adiabatic cooling rate and $w(z)\frac{\partial T(z)}{\partial z}$ the cooling rate due to vertical advection. The solar flux is calculated for diurnally averaged (i.e. zonally-averaged) insolation. We neglect the meridional advection of heat. As discussed by Achterberg et al. (2011) and Teanby et al. (2017), this term is expected to be ≤0.2 time the vertical advection term, based on the mass continuity equation and the observed horizontal temperature gradients, all the more at low latitudes where these temperature gradients are very small.

3.1 Solar flux

Our atmospheric grid consists of 41 pressure levels uniformly distributed in log-scale from 1.466 bar (surface pressure) to 0.133 μbar (around 650 km). The solar flux is calculated as a function of zenith angle θ_s and altitude from 2610 to 40000 cm^{-1} (3.8-0.25 μm) using a plane parallel radiative transfer code that incorporates the DISORT algorithm (Stamnes et al. 1988) with 8 streams to solve for scattering. The solar irradiance spectrum at 1 AU is the 2000 ASTM Standard Extraterrestrial Spectrum Reference E-490-00 (available at http://rredc.nrel.gov/solar/spectra/am0/). We consider opacity from methane and aerosols. Methane absorption is modeled from 2610 cm^{-1} (3.8 μm) to 25000 cm^{-1} (0.400 μm) using the correlated-*k* distribution method. From 2690 to 11850 cm^{-1}, absorption coefficients are calculated with a line-by-line radiative transfer model and molecular line parameters (positions, intensities, energy levels) from the TheoReTS database, which includes new accurate theoretical linelists of $^{12}CH_4$, $^{13}CH_4$ and $^{12}CH_3D$ (Rey et al. 2017). The assumed N_2-broadened halfwidths and far wing lineshape are described in Rey et al. The CH_3D/CH_4 ratio corresponds to D/H = 1.32×10^{-4} (Bézard et al. 2007). For each 40-cm^{-1} interval, a set of 16 *k*-coefficients, 8 for the interval [0:0.95] of the normalized frequency *g* and 8 for the interval [0.95:1.00], is calculated on a set of pressures and temperatures. Beyond 11850 cm^{-1}, we used the coefficients of the Voigt-Goody band model calculated by Karkoschka and Tomasko (2010, Table 4) based on methane transmission measurements from laboratory, Huygens and HST data. We then essentially proceeded as in Irwin et al. (1996) and generated, for each pressure and temperature of our set, 24 transmission (T_r) spectra with column densities (a) equally spaced in log space between a minimum value such as $T_r \approx 0.997$ and a maximum value such as $T_r \leq 0.01$. This function $T_r(a)$ was then fitted with an exponential sum characterized by 10-point Gaussian Legendre quadrature abscissae and weights, using a Levenberg-Marquardt non-linear least squares algorithm (Press et al. 1997). The first guess of the 10 k_i absorption coefficients was derived from the *k* distribution of a Malkmus-Lorentz band model (Eq. 12 of Irwin et al. 1996) having the *S* and *B* parameters given in Table 4 of Karkoschka and Tomasko (2010). The function $T_r(a)$ was actually fitted with the 10 parameters k_1 and (k_i-k_{i-1}), for i = 2,10, discarding the iterations leading to negative values of any of them, to ensure that they increase monotonically. We kept the original sampling of

Karkoschka and Tomasko (2010): 5 cm^{-1} in the interval 11850-19300 cm^{-1} and 25 cm^{-1} in the interval 19300-25000 cm^{-1}.

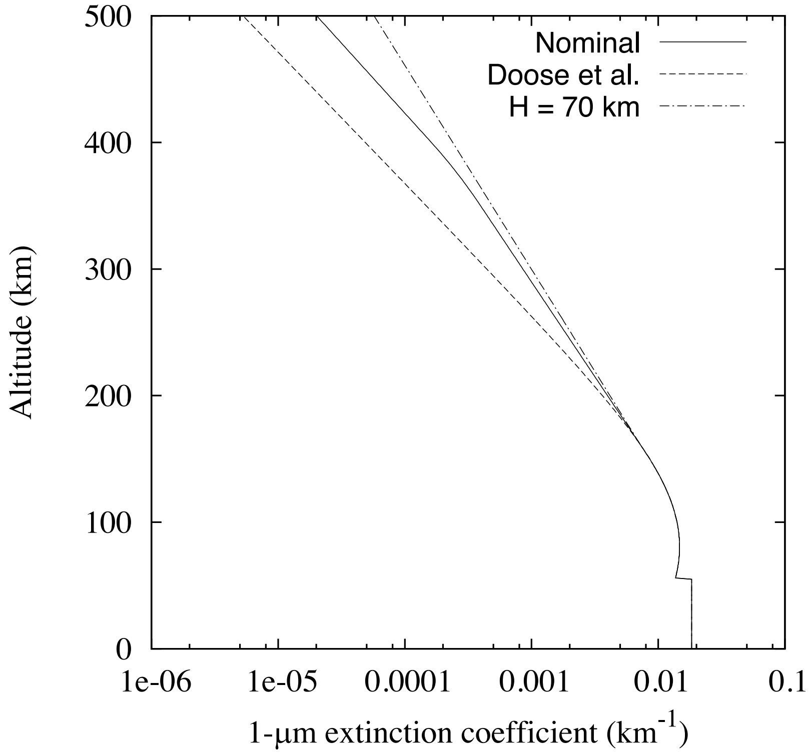

Figure 2: Haze extinction coefficient at 1 μm for our nominal model (solid line), Doose et al.'s (2016) model (dashed line) and one with a constant scale height of 70 km above 160 km (dash-dot line). In the thermal infrared range, at 1090 cm^{-1}, these extinction profiles are scaled by factors of 0.0103, 0.0113 and 0.0099 respectively.

The methane mole fraction profile used in the radiative transfer is that derived by Niemann et al. (2010) from the analysis of Huygens/GCMS in situ measurements, with a uniform mole fraction of 1.48×10^{-2} above 45 km. The temperature profile $T_0(p)$ is that retrieved by Vinatier et al. (2010a) from Cassini/CIRS limb and nadir spectra recorded near 20°S in March 2007, not far from the Huygens descent latitude.

The properties of the aerosol particles (single scattering albedo, phase function) were taken from the recent reanalysis of Huygens/DISR observations by Doose et al. (2016, Table 2) with information on the phase function from Tomasko et al. (2008c). Longward of 950 nm, we used the single scattering albedo derived by Hirtzig et al. (2013) from modeling of Cassini/VIMS data. We used the wavelength dependence of the extinction given in Table 2 of Doose et al. (2016). The vertical variation of the extinction at the Huygens site is constrained in detail between 0 and 144 km from the DISR measurements but only in average above this altitude. Doose et al. then added the additional constraint of the optical limb altitude as observed by Karkoschka and Lorenz (1997) to produce an analytical vertical profile of extinction characterized, in the stratosphere, by an optical depth scale height decreasing from large values below 80 km to a value of 65 km at 120 km and an asymptotic value of 45 km at very high altitudes (Fig. 2). Here we considered additional constraints from Cassini/CIRS measurements of the aerosol continuum emission in limb-viewing and nadir geometry between 600 and 1500 cm^{-1}. These measurements provide a vertical profile of the extinction at thermal wavelengths with a good precision between approximately 140 and 400 km (3-0.01 mbar) (Vinatier et al. 2010b, 2015). We used here the vertical dependence of the extinction determined from limb observations in January 2007 around 5°N (Vinatier et al. 2010a, b) and adapted by Vinatier et al. (2015) (dashed line in their Fig. 15). Their extinction profile has a scale height (H) of about ~65 km up to 350 km decreasing to ~48 km above 400 km. Our nominal profile for the haze extinction is then the Doose et al. profile up to 160 km, that we extend above with H = 65 km from 160 to 350 km, linearly decreasing to 48 km at 400 km (Fig. 2). The extinction profiles derived from CIRS measurements at equatorial and mid-latitudes show however a significant variability with latitude and year above 250 km (Vinatier et al. 2015, 2016). Although part of it may be an artifact due to uncertainties in the continuum calibration, especially at high altitudes (≥ 400 km), most of it is probably real, including the presence of the variable detached haze layer, as discussed in Vinatier et al. (2015). An average of the profiles observed in 2010-2012 between 20°N and 30°S (Fig. 15 of Vinatier et al. 2015) shows a vertical variation close to the Doose et al. profile up to 300 km and intermediate between our nominal profile and Doose et al. up to 400 km. On the other hand, observations at 26°S in January 2016 exhibit an approximately constant scale height H as large as 70 km between 200 and 500 km (Vinatier et al. 2016). We consider that the full Doose et al. profile and one having H = 70 km above 160 km represent a reasonable envelope of the actual extinction profiles at low latitudes (Fig. 2).

We assumed a Lambertian surface with the reflectivity inferred by Jacquemart et al. (2008) between 900 and 1600 nm from DISR/DLIS spectra taken at an altitude of 25 m and after landing of the Huygens probe. The surface reflectivity down to 400 nm was obtained from Eq. 5 of Karkoschka et al. (2012), giving the relative spectral variation of I/F derived from DISR/DLVS data after landing, and scaled with the Jacquemart et al. value at 900 nm. Between 250 and 400 nm, we assumed a linear variation of 4×10^{-4} nm^{-1} and, beyond 1600 nm, we used the Hirtzig et al. (2013) albedos derived from the methane windows in Cassini/VIMS spectra near the Huygens landing site. We account neither for the strong opposition effect seen in the phase function of Titan's surface (Karkoschka et al. 2012) nor for the fact that the surface at Huygens' landing site is darker than average at low latitudes. However, the influence of the surface reflectivity on the heating rate at stratospheric levels should be relatively low.

3.2 Thermal emission

Without scattering, the thermal flux at pressure level p is equal to:

$$F_{IR}(p) = 2\pi \int_0^\infty d\sigma \left[\int_{\tau_\sigma}^\infty B_\sigma\big(T(\tau'_\sigma)\big)E_2(\tau'_\sigma - \tau_\sigma)d\tau'_\sigma - \int_0^{\tau_\sigma} B_\sigma\big(T(\tau'_\sigma)\big)E_2(\tau_\sigma - \tau'_\sigma)d\tau'_\sigma\right], \quad (2)$$

where τ_σ is the optical depth at wavenumber σ and pressure level p, $B_\sigma(\tau_\sigma')$ is the Planck function at the temperature T of the level of optical depth τ_σ' and wavenumber σ, and E_2 is the second-order exponential integral ($E_2(x) = \int_1^{\infty} \frac{e^{-xt}}{t^2} dt$). The two terms in Eq. 2 represent the fluxes from respectively the upwelling and downwelling radiation at pressure level p. We calculate this integral from 20 to 1560 cm^{-1}, and divide it into n_k = 74 intervals of width $\delta\sigma$ = 20 cm^{-1}. Thermal emission from outside this spectral interval can be neglected in the energy budget. Our grid has n_p = 51 pressure levels uniformly distributed in log-scale from p_1 = 1.466 bar (surface pressure) to p_{n_p} = 0.1466 μbar (around 650 km). By linearizing the Planck function as a function of optical depth within each atmospheric layer of our grid [j, j+1], and assuming that the Planck function is constant over each spectral interval k of width $\delta\sigma$, i.e.:

$$B_{\sigma_k}(T(\tau'_\sigma)) = B_{\sigma_k}\left(T(p_j)\right)\frac{\tau_\sigma(p_{j+1})-\tau'_\sigma}{\tau_\sigma(p_{j+1})-\tau_\sigma(p_j)} + B_{\sigma_k}\left(T(p_{j+1})\right)\frac{\tau'_\sigma-\tau_\sigma(p_j)}{\tau_\sigma(p_{j+1})-\tau_\sigma(p_j)}, \quad (3)$$

Eq. 2 at a given pressure level p_i can be written out as summations over indices k and j as:

$$F_{IR}(p_i) = \pi\, \delta\sigma \sum_{k=1}^{n_k} \Bigg[\frac{B_{\sigma_k}(T(p_1))}{\delta\sigma} \int_{\sigma_k-\delta\sigma/2}^{\sigma_k+\delta\sigma/2} 2E_2\big(\tau_\sigma(p_1) - \tau_\sigma(p_i)\big)\, d\sigma +$$

$$\sum_{j=1}^{i-1} \frac{1}{\delta\sigma} \int_{\sigma_k-\delta\sigma/2}^{\sigma_k+\delta\sigma/2} d\sigma \int_{\tau_\sigma(p_{j+1})}^{\tau_\sigma(p_j)} B_{\sigma_k}\left(T(\tau'_\sigma)\right) 2E_2\big(\tau'_\sigma - \tau_\sigma(p_i)\big)\, d\tau'_\sigma -$$

$$\sum_{j=i}^{n_p-1} \frac{1}{\delta\sigma} \int_{\sigma_k-\delta\sigma/2}^{\sigma_k+\delta\sigma/2} d\sigma \int_{\tau_\sigma(p_{j+1})}^{\tau_\sigma(p_j)} B_{\sigma_k}\left(T(\tau'_\sigma)\right) 2E_2(\tau_\sigma(p_i) - \tau'_\sigma)\, d\tau'_\sigma\Bigg], \quad (4)$$

where the first term in the summation over k is the contribution from the surface, the second one that from atmospheric layers below level i and the third one that from atmospheric layers above level i. Combining Eqs. 3 and 4 allows us to express the flux at pressure level p_i as a linear combination of the Planck functions at the n_p pressure levels (p_j) and n_k wavenumbers (σ_k):

$$F_{IR}(p_i) = \pi\, \delta\sigma \sum_{k=1}^{n_k} \sum_{j=1}^{n_p} B_{\sigma_k}\left(T(p_j)\right) A_{i,j,k}, \quad (5)$$

where $A_{i,j,k}$ is a dimensionless coupling factor between levels p_i and p_j for the k^{th} frequency interval. We calculated this exchange matrix A for the reference temperature profile $T_0(p)$ (see above) and neglect its dependence on temperature in our seasonal model, given that it is generally much weaker than that of the Planck function.

The exchange matrix *A* was calculated through a line-by-line radiative transfer program that incorporates opacity from the collision-induced absorption (CIA) of N_2-H_2-CH_4 pairs, lines from CH_4, CH_3D, C_2H_6, C_2H_2, C_2H_4, CH_3C_2H, C_4H_2, C_3H_8, CO, CO_2 and HCN, and aerosols. Spectroscopic line parameters are described in Vinatier et al. (2010a) with, in addition, C_2H_6 lines in the 7-µm region from HITRAN2012 (Rothman et al. 2013), the CH_3C_2H bands around 15.5 and 30 µm from Geisa2011 (Jacquinet-Husson et al. 2011), and rotational lines from CH_4, CO and HCN as described in Lellouch et al. (2014). Line parameters of C_4H_2 bands were updated following Geisa2011. References for the CIA coefficients are given in Vinatier et al. (2007), with the N_2-CH_4 coefficients multiplied by a factor of 1.5, following Tomasko et al. (2008b). For the main haze opacity, we utilized the spectral dependence of the extinction cross section derived from Cassini/CIRS measurements by Vinatier et al. (2012) from 600 to 1500 cm^{-1} and by Anderson and Samuelson (2011) at shorter wavenumbers.

We used the vertical profiles of C_2H_6, C_2H_2, C_2H_4, CH_3C_2H, C_4H_2, C_3H_8, and HCN derived by Vinatier et al. (2010a) from limb measurements near 20°S in March 2007[1]. As for the calculation of the solar flux, the CH_4 profile is that of Niemann et al. (2010) and the CH_3D profile derives from D/H = 1.32×10^{-4} (Bézard et al. 2007). The CO_2 and CO mole fractions were held constant at 1.6×10^{-8} and 4.7×10^{-5} respectively (de Kok et al. 2007).

We assumed a uniform composition from 30°S to 30°N and constant throughout the mission. This is consistent with monitoring studies based on Cassini/CIRS nadir observations by

[1] Temperature and abundance profiles available from the Virtual European Solar and Planetary Access (VESPA) http://vespa.obspm.fr/planetary/data/epn/query/all/

Teanby et al. (2008) and Coustenis et al. (2013), which all show limited variations of composition at latitudes less than 30° in the ~2-10 mbar region. As shown later, C_2H_2, C_2H_6 and CH_4 are the main gaseous cooling agents. Compiling the C_2H_2 and C_2H_6 profiles retrieved from CIRS limb and nadir observations from 2007 to 2016 by Vinatier et al. (2010a, 2015, 2017b), we have calculated the standard deviation (SD) of the mole fractions in these sets at levels between 0.5 and 2 mbar. We found a SD of about 10% of the mean value for C_2H_6, which is about the 1-SD uncertainty of the retrievals, and 15-20% of the mean value for C_2H_2, which is only marginally larger than the retrieval uncertainty.

The vertical profile of haze extinction is the one described above to model the solar flux deposition, scaled to a value of 4.1×10^{-10} cm^{-1} at 200 km and 1090 cm^{-1} as derived by Vinatier et al. (2015) in the 30°S-20°N region in 2010-2012. We added the opacity of the nitrile haze characterized by Anderson and Samuelson (2011). The spectral dependence of this opacity at 15°S is given in Fig. 15 of that paper; it peaks at 160 cm^{-1} and is significant in the range 90-290 cm^{-1}. We used a normal optical depth of 0.0054 at 160 cm^{-1}, as derived by Anderson and Samuelson (2011) at 15°S, and the associated vertical profile of extinction, having a mass extinction coefficient peaking at 87.5 km with a full width at half maximum (FWHM) of 18.8 km.

3.3 Numerical aspects

Starting from the initial temperature profile $T_0(p)$, Eq. 1 is integrated through a time-marching scheme, with a constant step $\Delta\xi$ (typically 10^{-3}), ξ being related to the time t, Sun distance d and heliocentric longitude ϕ through the relations (Landau and Lifchitz 1969, Eqs. (15,10) and (15,11)):

$$t = \frac{T_{orb}}{2\pi}(\xi - e\sin\xi), \qquad 6(a)$$

$$d = a(1 - e\cos\xi), \tag{6(b)}$$

$$\cos\phi = \frac{\cos\xi - e}{1 - e\cos\xi}, \tag{6(c)}$$

where T_{orb} is Saturn's orbital period, e its orbit eccentricity, a its semi-major axis, with the origin of time and longitude taken at perihelion ($\xi = 0$, $t = 0$, $\phi = 0$). Note that the heliocentric longitude with an origin at northern spring equinox L_s is then equal to $\phi + L_s^0$, L_s^0 being the value of L_s at perihelion. The solar declination δ_s is given by:

$$\sin\delta_s = \sin\delta\sin L_s, \tag{6(d)}$$

where δ is Saturn's obliquity.

The time-marching integration is run for long enough so that the influence of the initial profile $T_0(p)$ has vanished at the end. At each time step, the diurnally averaged solar flux is derived for the corresponding solar declination and Sun-Saturn distance by integrating over daytime and interpolating as a function of $\cos(\theta_s)$ from the solar fluxes pre-calculated for zenith angles θ_s = 0, 30, 50, 60, 70, 80 and 85° (Section 3.1). The thermal flux is calculated from Eq. 5, assuming as a boundary condition a constant surface temperature of 93.5 K and emissivity of 1.0. Radiative cooling and heating rates are then calculated on the atmospheric pressure grid by differentiation of the solar and thermal fluxes. After adding the adiabatic and advective cooling/heating terms in Eq. 1 to the radiative terms, the variation of temperature ΔT at each level is calculated from Eq. 1 as Δt times the sum of these three energy terms, and the process is iterated till the desired date.

4. Results

4.1 Heating and cooling rates in the stratosphere

Figure 3 shows, at three different pressure levels, the spectral heating rate h_λ, giving the wavelength dependence of the absorbed solar energy (the solar heating rate in Eq. 1 is $h = \int h_\lambda d\lambda$). At pressures less than ~5 mbar, heating is dominated by aerosol absorption of solar radiation at wavelengths below 0.8 μm, with a peak around 0.4 μm at 0.1 mbar and 0.45 μm at 1 mbar. At 10 mbar, the strong methane bands between 0.8 and 3.7 μm provide substantial additional heating. In this region, methane and aerosol absorption provide comparable contributions to the solar heating while, at deeper levels, methane absorption dominates.

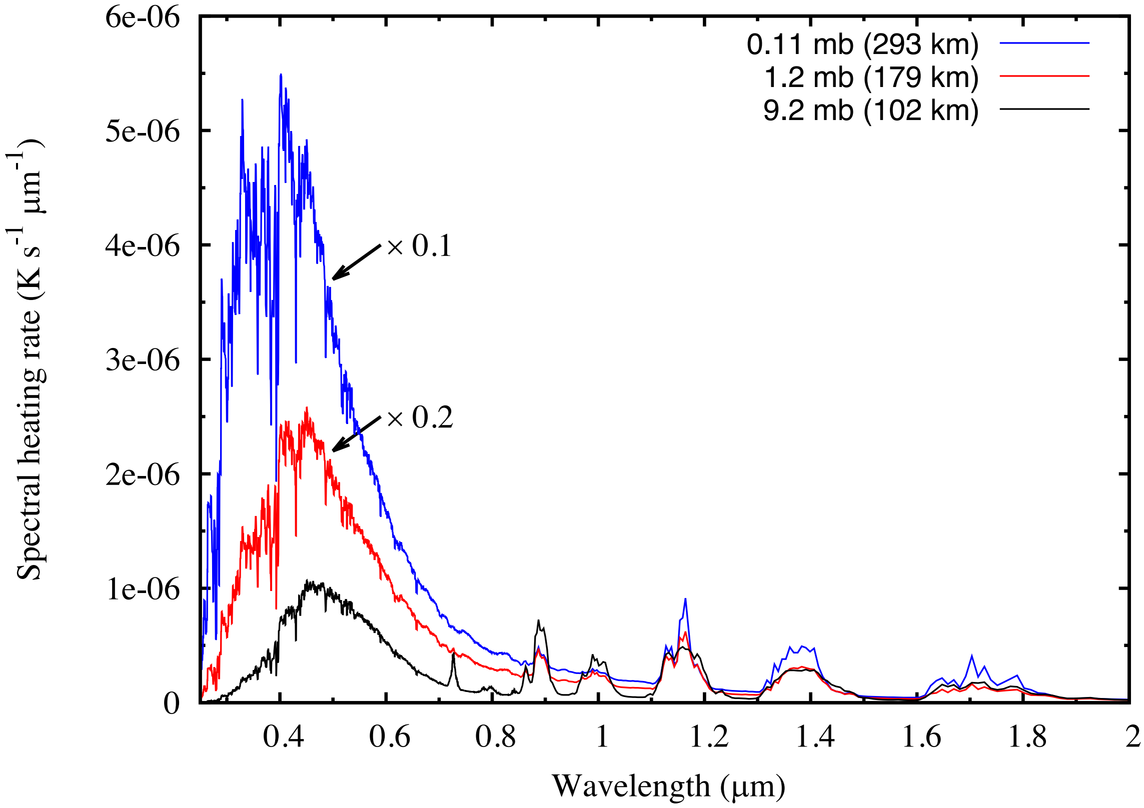

Figure 3: Spectral heating rate h_λ giving, as a function of wavelength, the contribution per unit wavelength to the day-averaged solar heating rate at three different atmospheric levels. For clarity, h_λ at 0.11 mbar is multiplied by 0.1 and h_λ at 1.2 mbar by 0.2. The solar heating rate is integrated from 0.25 to 3.8 μm. Insolation conditions correspond to 20°S and March 2007.

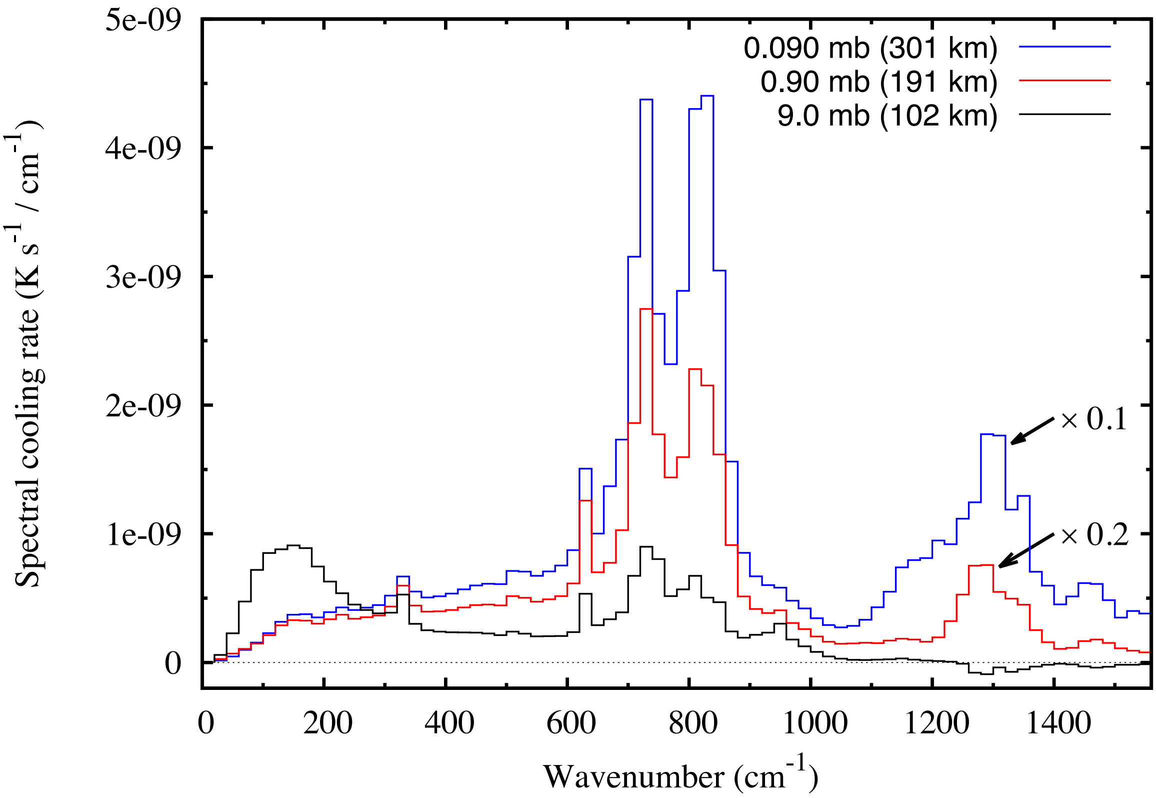

Figure 4: Spectral distribution of the cooling rate c_σ, averaged over 20-cm^{-1} bins, giving, as a function of wavenumber, the contribution to the radiative cooling rate at three different atmospheric levels. For clarity, c_σ at 0.09 mbar is multiplied by 0.1 and c_σ at 0.9 mbar by 0.2. The temperature profile pertains to 20°S and March 2007.

The spectral distribution of the radiative cooling rate (c_σ), averaged over 20-cm-1 intervals, is shown in Fig. 4 at three different levels in the stratosphere. The cooling rate c in Eq. 1 is the integral over wavenumber of c_σ: $c = \int c_\sigma d\sigma$. The most efficient gaseous coolers are ethane (820 cm^{-1}), acetylene (730 cm^{-1}) and, above the ~5 mbar level, methane (1300 cm^{-1}). Note that at (and below) the 9-mbar level, the methane band heats the atmosphere from above. Substantial cooling in the stratosphere arises from the continuous aerosol opacity. As noted earlier by Tomasko et al. (2008b), the cooling effects of gas and aerosol emission are of the same order. Note, in the 9-mbar cooling rate spectrum, the contribution from the nitrile haze peaking at 160 cm^{-1} (Anderson and Samuelson 2011).

In Fig. 5, we show the heating and cooling rate profiles calculated with our model for the composition and temperature profile derived from CIRS measurements near 20°S in March 2007. Both profiles steadily decrease with depth, by more than 3 orders of magnitude from the lower mesosphere to the lower troposphere. In the whole region 0.1-5 mbar, best constrained by CIRS measurements in terms of temperature, haze and composition, the heating and cooling rate profiles are remarkably similar, the former being regularly 20-35% larger than the latter. The difference between them varies between 3×10^{-6} K s^{-1} at 0.1 mbar and 2×10^{-7} K s^{-1} at 5 mbar. As the observed temperature variation around 2007 is less than 1 K $year^{-1}$ (Fig. 1), i.e. $< 3 \times 10^{-8}$ K s^{-1}, the energy balance equation (Eq. 1) implies that this difference has to be balanced by adiabatic cooling. This leads to upward velocities decreasing from 0.25 cm s^{-1} at 0.1 mbar to 0.09 cm s^{-1} at 1 mbar and 0.014 cm s^{-1} at 5 mbar.

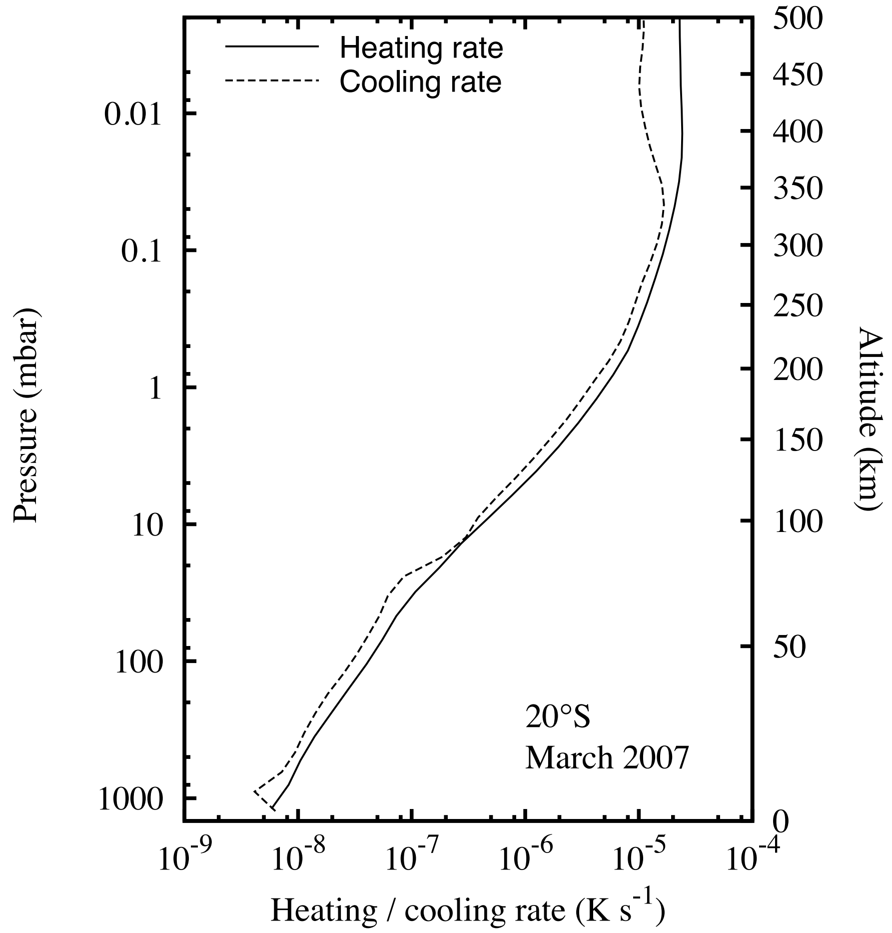

Figure 5: Heating (solid line) and cooling (dashed line) rate profiles calculated with our model using the temperature profile retrieved from CIRS measurements at 20°S in March 2007. The heating rate profile corresponds to day-averaged conditions and insolation parameters for March 2007.

Around 15 mbar (85 km), which corresponds to the peak of the nitrile haze, the cooling and heating rates are almost equal. Just below, around 25 mbar (71 km), the heating rate exceeds the cooling rate by about 70%. This region corresponds to the fall-off of the C_2H_6 and C_2H_2 mixing ratios due to condensation, these two gases being important infrared radiators in the whole stratosphere. Below the 50-mbar level, in the troposphere, the heating rate is about 40% larger than the cooling rate. Note that no information from CIRS data is available using the ν_4 CH_4 band below the ~ 10-mbar level, and the temperature profile then joins the Huygens/HASI *in situ* measurements at 10°S (Fulchignoni et al. 2005). Above the ~ 0.03-mbar level, the heating rate is about twice the cooling rate, which would call from Eq. 1 for an upward velocity w of about 1.5 cm s^{-1}. However, this estimation is very uncertain due to the poorly known haze density in this region.

4.2 Radiative relaxation times

Evaluation of radiative time constants is important to investigate the response of Titan's atmosphere to various perturbations, such as the diurnal and seasonal cycles of insolation, or atmospheric waves. As discussed by Flasar et al. (2014), the radiative time constant (τ_r) is the characteristic time for radiatively damping out a small perturbation from the equilibrium state, keeping unchanged all other energy terms such as solar and dynamical heating. From Eq. 1, τ_r is formally equal to the inverse of the derivative of the cooling rate with respect to temperature:

$$\tau_r(z) = 1 / \frac{\partial c(z)}{\partial T(z)} \qquad (7)$$

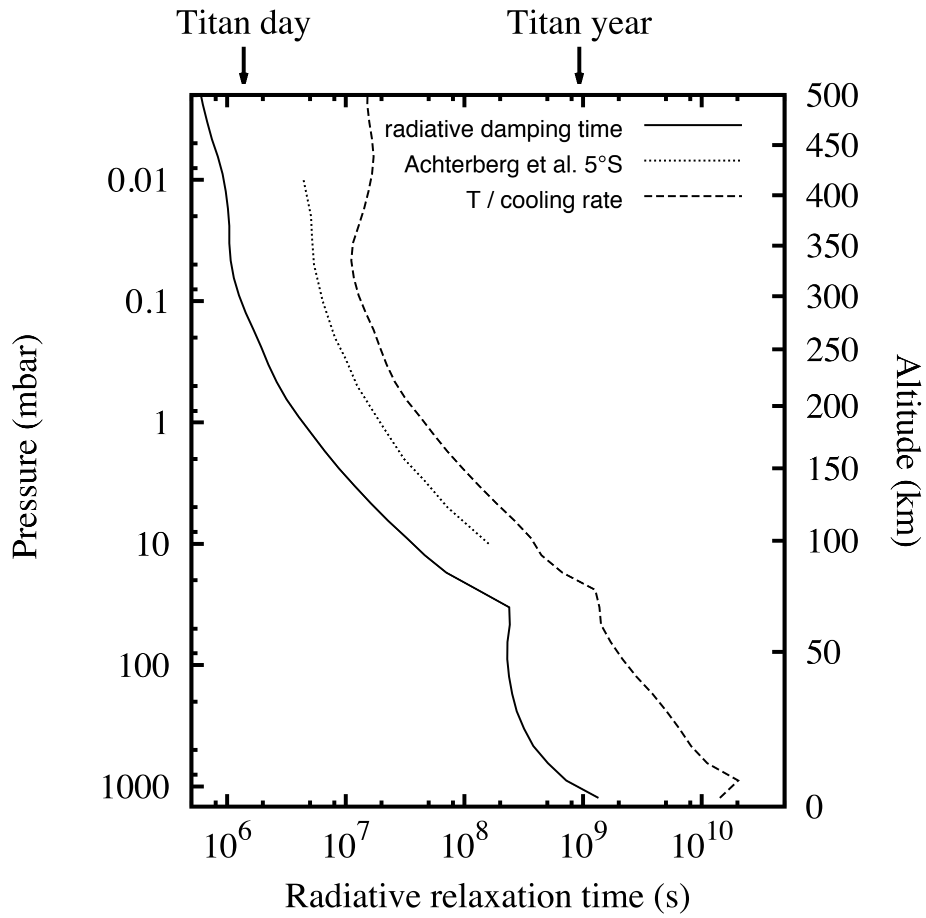

Figure 6: Vertical profiles of radiative relaxation time in Titan's atmosphere. The solid line corresponds to damping out a Gaussian temperature perturbation having a full width at half maximum of one pressure scale height. The dotted line shows the radiative time constant calculated by Achterberg et al. (2011) at 5°S using the direct cooling-to-space approximation for the radiative cooling. The dashed line represents the temperature divided by the cooling rate, following the approach of Strobel et al. (2009).

However, $c(z)$ in a given layer depends to some extent, through exchange terms, on the temperature outside this layer so that the vertical shape of the assumed perturbation has to be specified. We assumed here a Gaussian perturbation having a FWHM of 1 pressure scale height and centered in a layer $[p_i{:}p_{i+1}]$. Doing so, $\frac{\partial c(z)}{\partial T(z)}$ can be calculated from Eq. 5 as a linear combination of terms in the form $(A_{i+1,j,k} - A_{i,j,k})\dfrac{\partial B_{\sigma_k}\left[T(p_j)\right]}{\partial T(p_j)}$ where j runs over the perturbed levels with appropriate weighting. The resulting profile of τ_r is shown in Fig. 6 as a solid line.

The radiative time constant readily increases with depth from less than 1 Titan day above the 0.1-mbar level to about 1 Titan year in the lowest layers of the troposphere. In the range 0.1-5 mbar, in which we are mostly interested here, the radiative time constant varies between 0.0015 and 0.02 Titan year, implying that the stratosphere can respond radiatively to the seasonally-varying insolation with negligible time lag. We also made a calculation for a perturbation having a twice larger FWHM (2 scale heights). The resulting time constants are then ~ 25% larger in the stratosphere and ~ 60% in the troposphere below the 300-mbar level.

In Fig. 6, we also show the radiative cooling timescale calculated by Achterberg et al. (2011) at 5°S using the direct cooling-to-space approximation and including opacity from CH_4, C_2H_2 and C_2H_6. Their time constants are 4-5 times larger than those inferred in this work. A factor of ~ 2 is likely due to the lack of aerosols and other gases in their calculations and the remaining difference from ignoring the exchange terms, as discussed in Section 5. We also plotted in Fig. 6, the ratio of temperature to cooling rate ($T(z)/c(z)$), which yields a simpler estimate of the radiative timescale. As can be seen from Eq. 1, rather than relevant to damping of a temperature perturbation, this time constant pertains to a case in which the solar heating is turned off (as well as the dynamical term). This is the approach that was used by Strobel et al. (2009) to compute the radiative timescale. Figure 6 shows that, doing so, the radiative damping time is overestimated typically by a factor of 10.

4.3 Temperature profile at 6°N

We first compare the predictions of our seasonal radiative model, with no adiabatic heating/cooling, to the temperature profile retrieved near 6°N around northern spring equinox (See Section 2), a region where seasonal variations of insolation are minimal. Figure 7 shows the temperature profile calculated with the three haze profiles of Fig. 2. Temperatures in these models essentially differ above 200 km due to different assumptions on the vertical profile of aerosol extinction. The warmest profile is associated with the largest aerosol number extinction profile and vice versa, confirming that aerosol heating from scattering and absorption of solar radiation dominates over their cooling effect due to thermal emission. The difference between the extreme profiles increases from 7 K at 0.1 mbar to 20 K at 0.001 mbar.

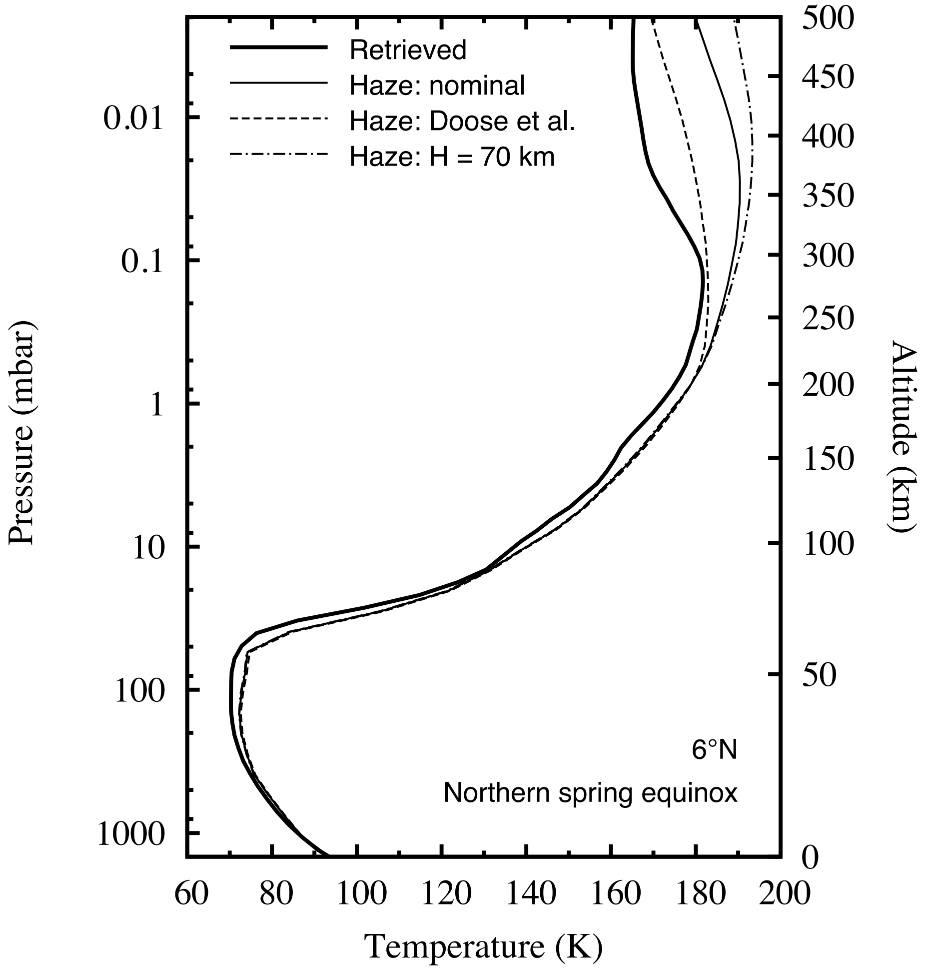

Figure 7: Comparison of a temperature profile retrieved from Cassini/CIRS measurements around 6°N and northern spring equinox (thick solid line) with radiative model profiles calculated for the three haze models in Fig. 2. No dynamical term is included in the energy equation.

Whatever haze profile is used, the radiative model profile is warmer than the retrieved one at all levels except around 15 mbar (85 km). Note that below 5 mbar, the profile is not constrained by Cassini/CIRS measurements but essentially represents the Huygens/HASI profile (10°S, January 2005). To bring the calculated and observed profiles closer, it is necessary to add adiabatic cooling. For our nominal haze model, we find that a constant vertical velocity, expressed in pressure coordinates ($\frac{dP}{dt} = -\rho g w$, where ρ is the atmospheric density), of ≈ -1.3 Pa per Titan day up to the 0.6-mbar level, slightly decreasing in amplitude at higher altitudes to reach ≈ -1.0 Pa per Titan at 0.02 mbar, allows us to reproduce fairly well the observed profile from the 0.05-mbar level down to the troposphere (Fig. 8, dashed line). The largest discrepancy occurs around 15 mbar, where the model profile is 5 K colder than the Huygens profile.

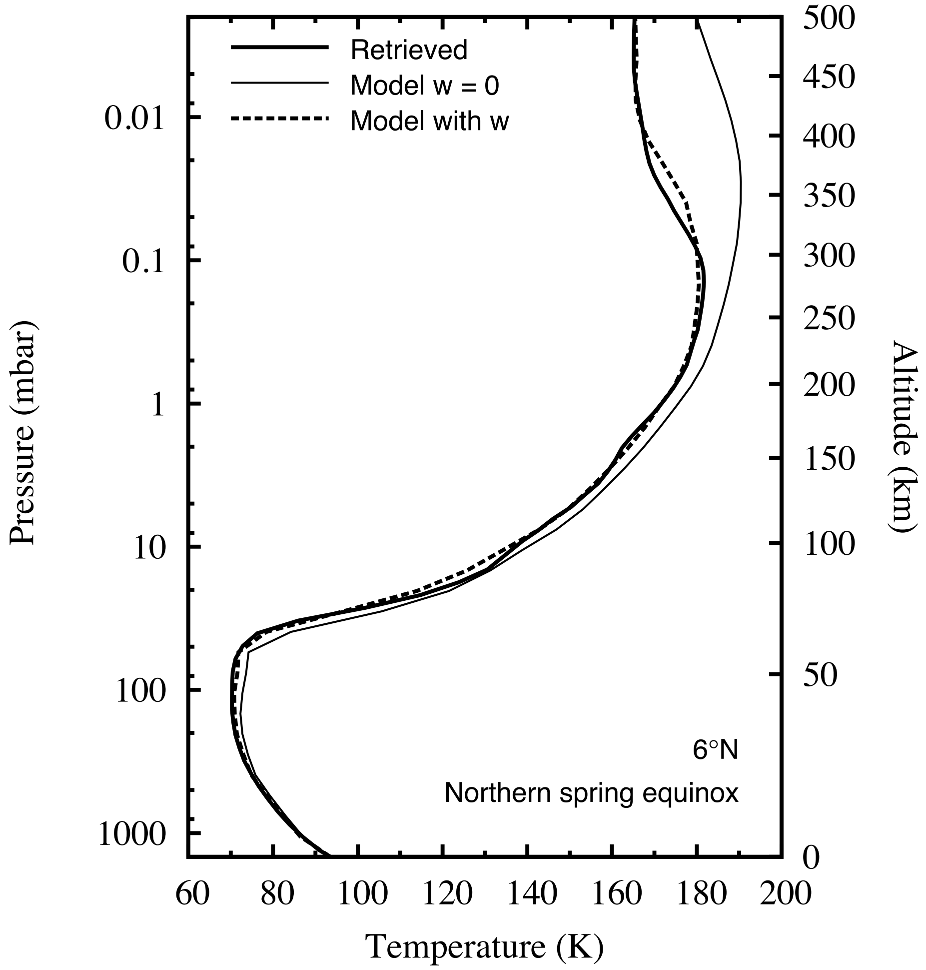

Figure 8: Comparison of a temperature profile retrieved from Cassini/CIRS measurements around 6°N and northern spring equinox (thick solid line) with two radiative model profiles using the nominal haze model. The thin solid line shows the case with no additional adiabatic heating (same as in Fig. 7). The dashed line shows a model with a constant velocity below the 0.6-mbar level, when expressed in pressure coordinates, equal to -1.3 Pa / Titan day, decreasing to -1.0 Pa / Titan day at 0.02 mbar and -0.5 Pa / Titan day at 0.01 mbar (Fig. 9).

This velocity profile corresponds to an upward vertical velocity w in the range 0.03-0.05 cm s^{-1} at 1 mbar, taking into account a 1 K uncertainty (Fig. 9), which corresponds to the dispersion in our 6°N temperature profile selection (Section 2). w varies as $(\rho g)^{-1}$ below the 0.6-mbar level and as $(\rho g)^{-0.92}$ in the 0.6-0.02 mbar range. At higher levels, the velocity is set so that it varies as $(\rho g)^{-0.1}$ from 0.02 to 0.01 mbar, and as $(\rho g)^{0.35}$ above (Fig. 9). The approximate constancy of $\frac{dP}{dt}$ below the 0.02-mbar level suggests only weak divergence of the upward flow in the stratosphere, while the decrease of $\frac{dP}{dt}$ at higher levels implies stronger divergence, i.e. horizontal poleward motion. However, this conclusion is not firm due uncertainties in the haze profile. It still holds if we use the upper limit for the haze density ("H = 70 km" case) but not for the lower limit (Doose et al. profile), in which case a strong decrease of $\frac{dP}{dt}$ above the ≈ 1 mbar level is required to reproduce the 6°N temperature profile (Fig. 9).

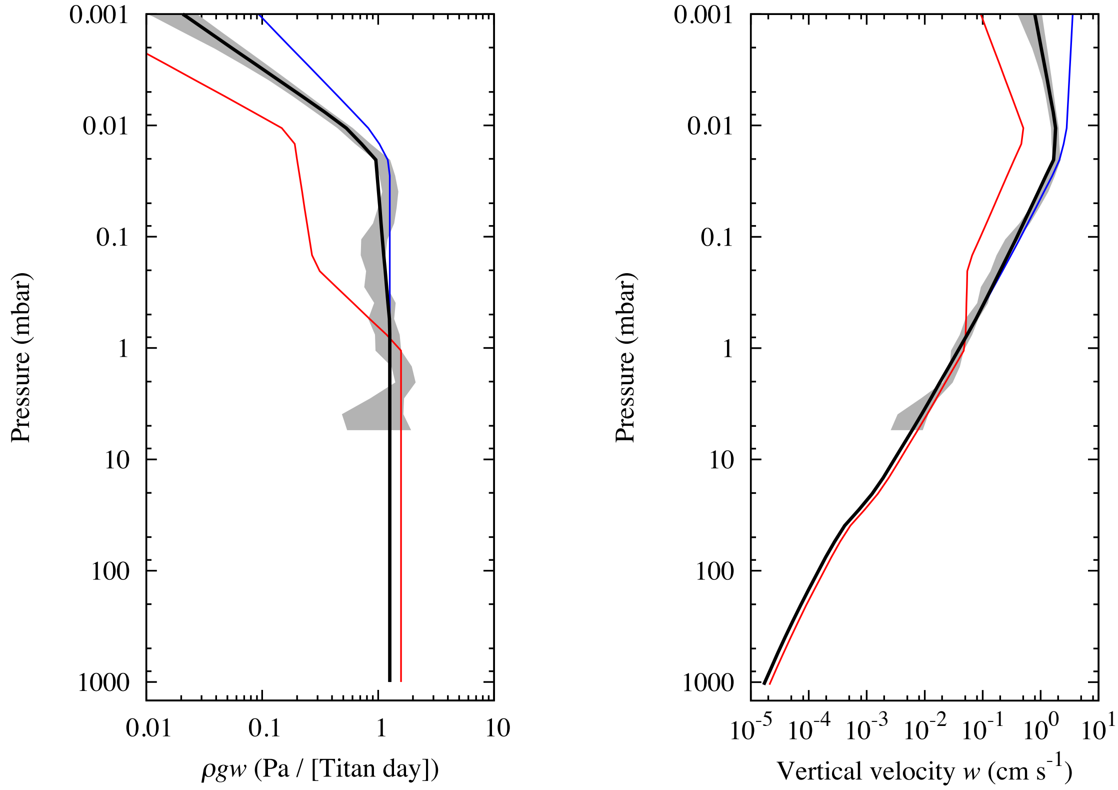

Figure 9: Upward velocity profile used to model the temperature profile retrieved at 6°N around equinox, given in pressure units per Titan day (left panel) and in cm s^{-1} (right panel). The black line corresponds to the model with the nominal haze profile that yields the best fit of the temperature profile (Fig. 8), while the red line corresponds to the Doose et al. profile and the blue line to the "H = 70 km" haze profile shown in Fig. 2. The grey area around the best fit velocity profile corresponds to a temperature uncertainty taken as the standard deviation of our 6°N temperature profile selection given in Section 2.

4.4 Seasonal variations of temperature at 1 mbar

We first investigate here the variations of temperatures at 1 mbar derived from Cassini/CIRS in the equatorial region from 2004 to 2016 (Fig. 1). Figure 10 shows our model predictions using a constant upward velocity of 0.040 cm s^{-1} at 1 mbar as derived above around 6°N near northern spring equinox. This model predicts a ~7 K drop between pre-equinox (2006-2008) and 2016. This variation is due to Saturn's eccentricity of 0.054, which modulates the distance to the Sun and thus the solar flux striking the Saturn system. A model with zero eccentricity (dashed line in Fig. 10) shows a shallow maximum around mid 2010 and similar temperatures in 2006 and 2016. In contrast, the model accounting for the orbital eccentricity predicts a maximum around 2007, between the perihelion (July 2003) and the equinox (August 2009), followed by a decrease due to the increasing distance with the Sun. In fact, while the temperatures after 2012 are then correctly reproduced by this model, the contrast between pre-equinox and 2016 (~7 K) is even larger than the observed value of ~4 K. Increasing the vertical velocity in the model uniformly shifts the calculated temperatures and does not help to reduce the contrast (Fig. 10). To better reproduce the observations, a modulation of the vertical velocity, i.e. of the adiabatic cooling, is required. We chose to do so by simply adding a sine function of the heliocentric longitude L_s to the velocity, which then becomes:

$$w(p) = w_c(p) + w_m(p) \sin L_s \quad (8)$$

At the 1-mbar level, w_c = 0.055 cm s^{-1} and w_m = 0.020 cm s^{-1} allows us to reproduce relatively well the observed variation (red line in Fig. 10). The vertical velocity at 1 mbar then varies seasonally between 0.035 and 0.075 cm s^{-1} but is always positive (upward), meaning dynamical cooling of the equatorial region all year through. Note that the vertical profile of w_c used here and shown in Fig. 11 differs somewhat from those used at 6°N in Section 4.3 because it was adjusted to better match the temperatures at 0.2, 0.5, 1, 2 and 4 mbar retrieved by Achterberg et al. (in preparation) and shown in Section 4.6.

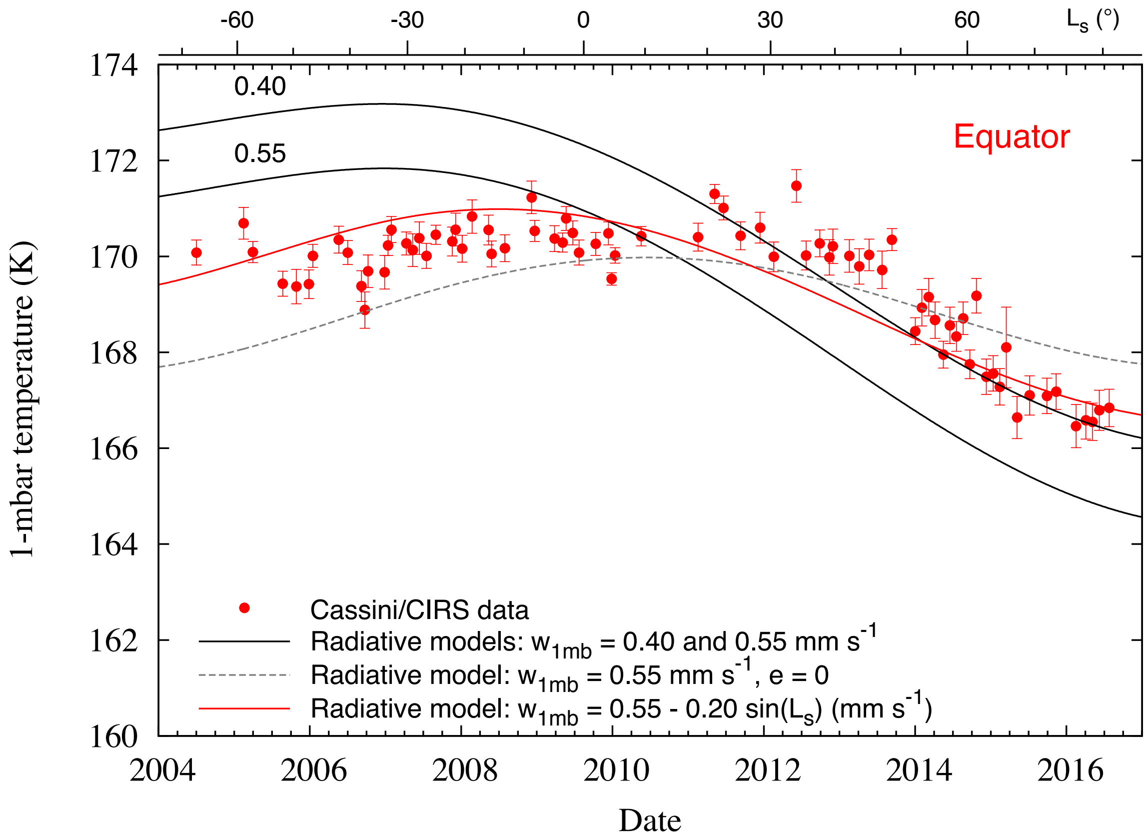

Figure 10: Time variation of 1-mbar temperatures in the equatorial region are compared with predictions from our seasonal radiative model. Solid lines represent models with constant-with-time upward velocity profiles having w(1 mbar) = 0.040 and 0.055 cm s^{-1}. The dashed line represents a model with w = 0.055 cm s^{-1} and the orbital eccentricity set to zero. The red line represents a model with a seasonally-varying vertical velocity profile: w(1 mbar) = 0.055 – 0.020 sin(L_s) cm s^{-1}, where L_s is the heliocentric longitude.

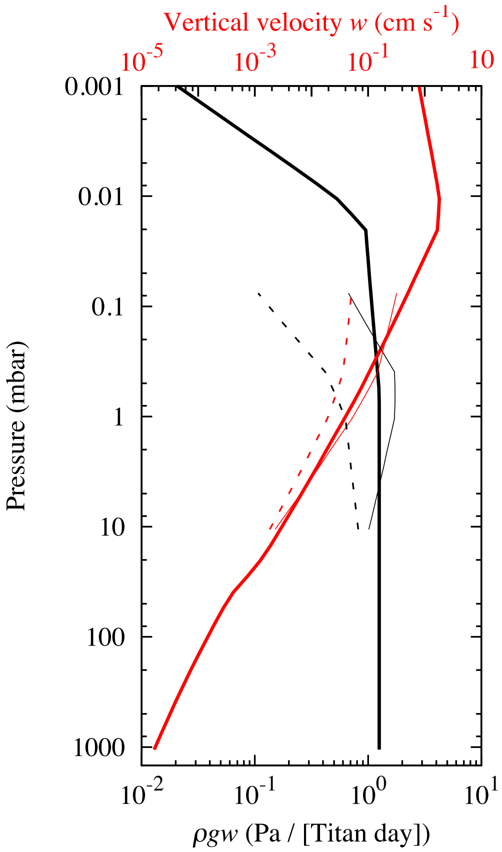

Figure 11: Thick solid lines: upward velocity profile used to model the temperature profile retrieved at 6°N around equinox (Fig. 8), given in pressure units per Titan day (black) and in cm s-1 (red). Thin solid lines: year-averaged upward velocity profile w_c used to model the seasonal temperature variations at the equator as retrieved by CIRS (Figs. 10 and 15). Thin dashed lines: amplitude of the sine term of this upward velocity profile w_m. See Eq. 8. Note that w_c and w_m are constrained from CIRS observations only from 0.2 to 4 mbar.

We then applied our model to latitudes 30°N and S where seasonal variations of insolation are more pronounced. Figure 12 shows the predicted variations of temperature at 1 mbar over a full Saturnian year (29.46 years), using a constant-with-time upward velocity profile (with $w = 0.055$ cm s^{-1} at 1 mbar). Such a model predicts large variations of temperature as a response to the seasonally-varying insolation with peak-to-peak amplitudes of 33 K at 30°S and 19 K at 30°N. The amplitudes are stronger in the southern hemisphere than in the northern due to the orbital eccentricity, the perihelion occurring less than a year before southern summer solstice. Clearly, the predicted variations are much stronger than observed by Cassini since 2004 (Fig. 12). Most noticeable in this comparison is the observed decrease of the 1-mbar temperature since 2013 at 30°N, which is at odds with the increase predicted by the radiative model as a result of increasing insolation. This behavior can only be explained by an increase of the dynamical cooling with time at this latitude. More generally, the observed variations at 30°N and S point to dynamics acting to counterbalance the seasonal variations in the solar heating. This means dynamical heating, or reduced cooling, in winter and enhanced dynamical cooling in summer. To model this pattern in a simple way, we proceeded as above and modulated the vertical velocity in the form of Eq. 8. The best fits to the data that we obtained are shown in Figs. 13-14 with the corresponding values of w_c and w_m given in Table 1. As can be seen, this simple model is able to reproduce the observed variations relatively well.

Table 1. Model parameters for the vertical velocity profile[1]

Latitude	w_c (1 mbar) (cm s^{-1})	w_m (1 mbar) (cm s^{-1})
Equator	+0.055	-0.020
30°N	+0.063	+0.075
30°S	+0.053	-0.105

Pressure range (mbar)	α_c	α_m
< 0.01	-0.40	-0.40
0.01-0.025	0.20	0.20
0.025-0.4	0.45	0.30
0.4-1	1.0	0.60
> 1	1.2	0.90

[1]: upward velocity is modeled as $w(p) = w_c(p) + w_m(p)\sin L_s$, and w_c (resp. w_m) varies as $(\rho g)^{-\alpha_c}$ (resp. $(\rho g)^{-\alpha_m}$) in a given pressure range.

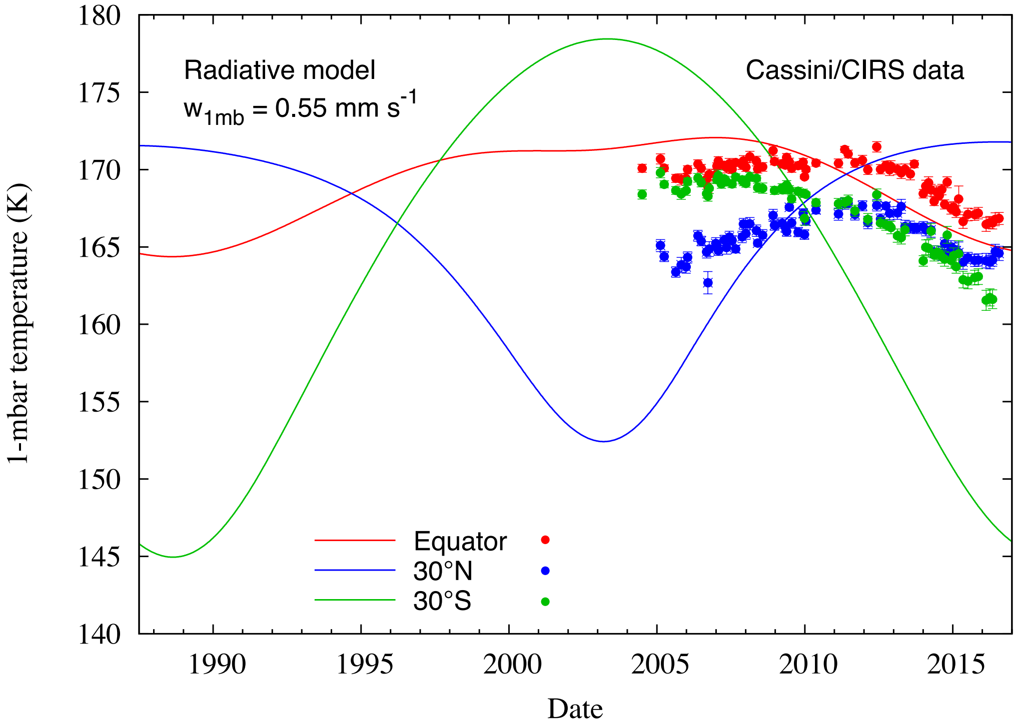

Figure 12: Time variation of 1-mbar temperatures at 0°, 30°N and 30°S predicted by the seasonal radiative model using a constant-with-time upward velocity profile with w(1 mbar) = 0.055 cm s^{-1}. Data retrieved from Cassini/CIRS measurements (Fig. 1) are overplotted for comparison.

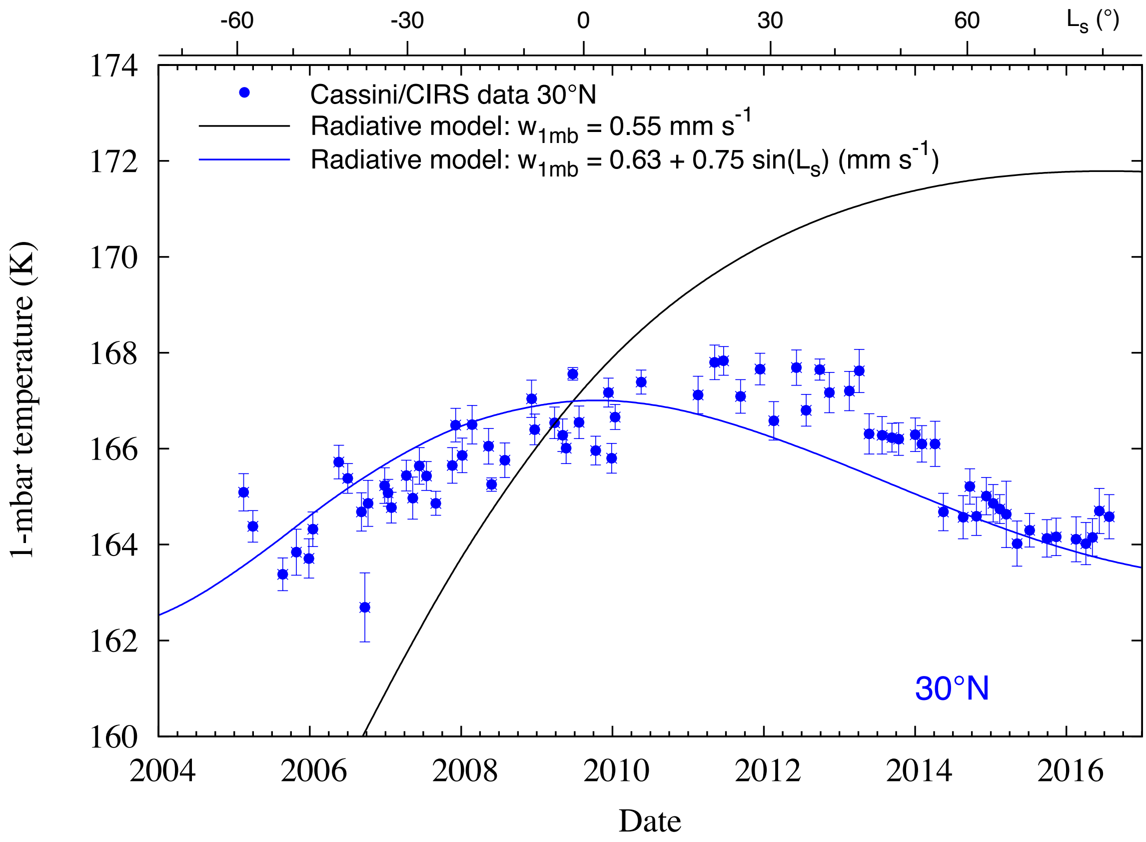

Figure 13: Time variation of 1-mbar temperatures at 30°N predicted by the seasonal radiative model are compared with data retrieved from Cassini/CIRS measurements (Fig. 1). Black line: constant-with-time vertical velocity; colored line: vertical velocity varying with solar longitude (see parameters in Table 1).

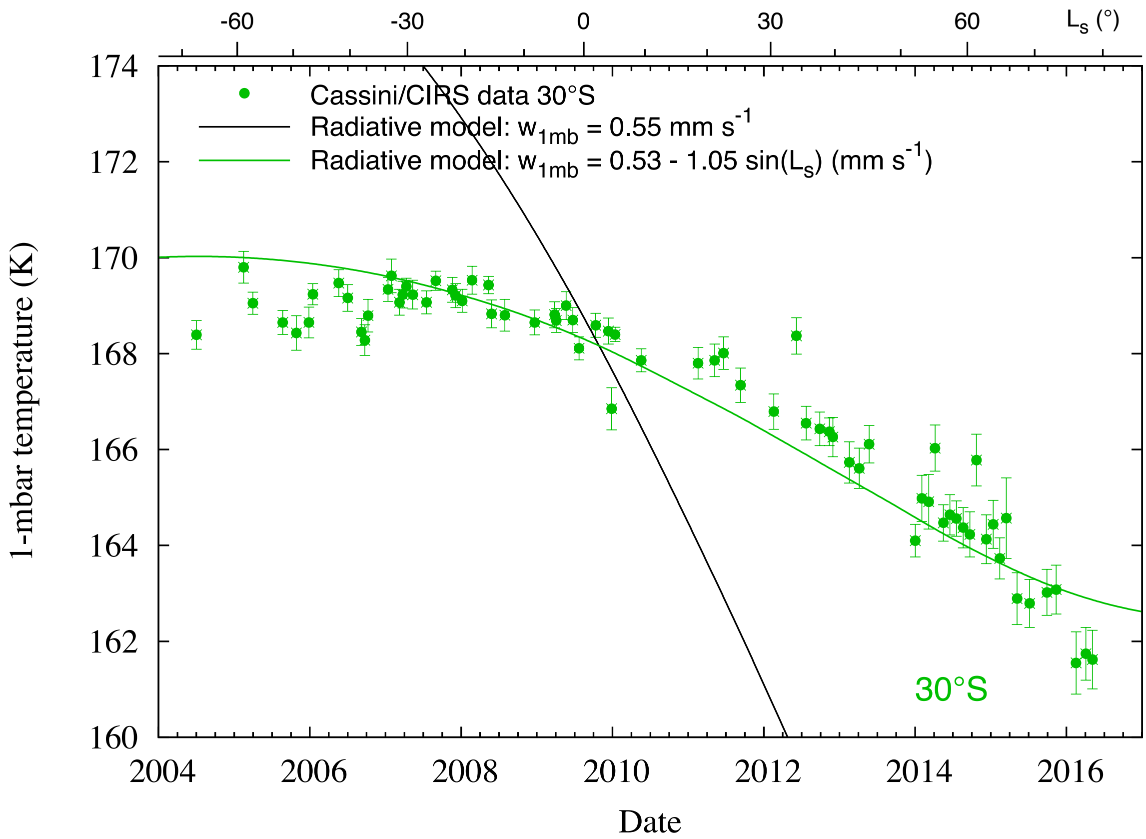

Figure 14: Same as Fig. 12 for 30°S.

4.5 Seasonal variations of temperature at other levels

In Section 4.4, we focused on the 1-mbar level, which is the region best constrained by Cassini/CIRS observations in terms of haze properties and temperature, and we have tuned our model to best reproduce the data at this level. In this section, we extend our modelling up to 0.2 mbar and down to 4 mbar, where temperature information is also available (Fig. 15). To do so, we used a vertical velocity profile $w(p)$ varying as $(\rho g)^{-\alpha}$ in a given pressure range as indicated in Table 1 and shown in Fig. 9 at the equator. As we intend to keep a smooth variation for $w(p)$, we did not try to match exactly the average temperature at a given pressure level apart from that at 1 mbar. We then have typical discrepancies of ±3 K on the average temperatures which may be due to uncertainties in our haze model above ~0.4 mbar (Fig. 7) and possibly systematic uncertainties in the temperature retrievals below ~2 mbar. We are therefore more interested here in the seasonal variations of temperature at a given level than in their absolute mean values.

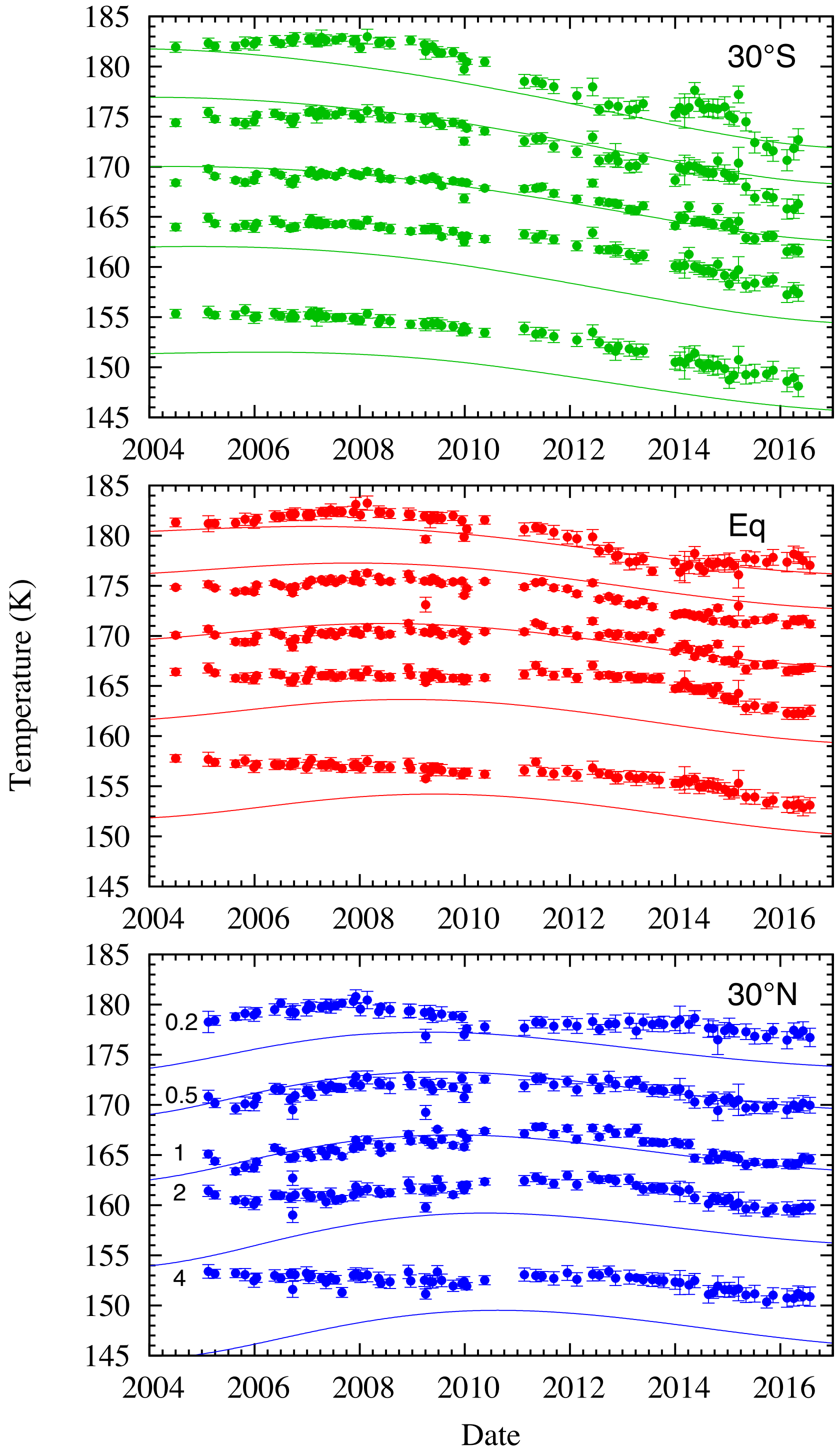

Figure 15: Time variation of temperatures at 0.2, 0.5, 1, 2 and 4 mbar predicted by the seasonal radiative model (colored lines) are compared with data retrieved from Cassini/CIRS measurements at 30°S, equator and 30°N. In this model, the vertical velocity varies as an affine function of sin L_s (see parameters in Table 1).

In Fig. 15, we show the seasonal variations of temperature predicted by our model for different pressure levels at 0, 30°N and 30°S. In these "best-fit" models, the vertical variation of the constant and sine components of the velocity profile were chosen to reproduce satisfactorily the observed seasonal variations at the three latitudes simultaneously (only one set of parameters for all latitudes, given in Table 1). On the other hand, the velocity terms w_c and w_m at 1 mbar were adjusted at each latitude to best reproduce the seasonal variations at this level, as discussed in Section 4.4. The CIRS-derived variations are overall fairly well reproduced except noticeably at 4 mbar where the steady decrease of temperature at the equator and at 30°N before equinox (2009) is not predicted by the model.

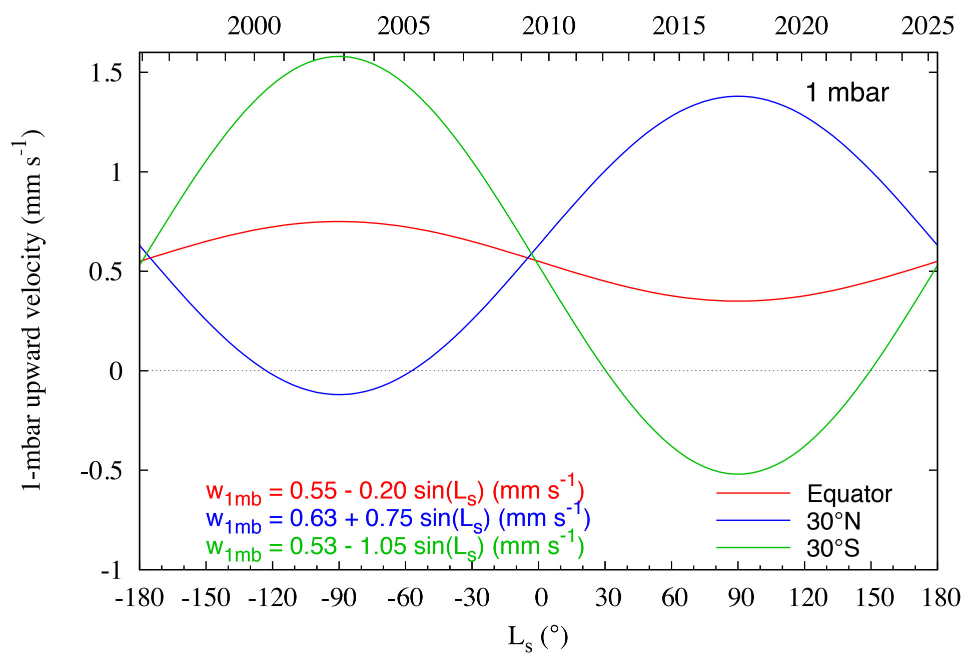

Figure 16: Time variation of the 1-mbar model upward velocity at 0°, 30°N and 30°S as a function of heliocentric longitude (lower scale) and year (upper scale).

The seasonal variation of the model velocity profile w at 1 mbar is shown in Fig. 16 for the three latitudes. The seasonal variation at other pressure levels can be obtained from the parameters in Table 1. The vertical dependence of the two components (w_c and w_m in Eq. 8) is illustrated in Fig. 11.

5. Discussion

5.1 Heating and cooling rates

Tomasko et al. (2008b) computed the solar heating rate at Huygens probe-landing latitude, averaged over longitude, using the haze model derived from DISR measurements by Tomasko et al. (2008c) and methane absorption coefficients simultaneously derived from DISR measurements (Tomasko et al. 2008a). The solar heating rates we derived at 20°S in March 2007 do not differ from those of Tomasko et al. by more than ±25% in the range 10-170 km. The largest differences occur at 10 and 170 km where our heating rate is some 20% larger and near 90 km where our heating rate is 25% smaller. We regard these differences as acceptable given the difference in the haze model, which was recently updated by Doose et al. (2016), and in the methane absorption, which we calculate using the ab initio TheoReTS database (Rey et al. 2017).

Cooling rates corresponding to the temperature, gas and haze profiles derived from Huygens and Cassini/CIRS data were also calculated by Tomasko et al. (2008b). Our cooling rate profile agree with theirs to within ±20% in the whole altitude range 10-400 km, with the maximum discrepancy occurring near 10 km (ours is 20% smaller) and 70 km (ours is 20% larger).

Comparing the heating and cooling rates calculated at the Huygens landing site, Tomasko et al. (2008b) concluded that the former exceeds the latter by a maximum of 0.5 K per Titan day near 120-130 km and that the excess decreases strongly below and above this altitude. At 125 km, we derive 0.4 K / Titan day, in good agreement with Tomasko et al. Below this altitude, we also find that the net radiative heating minus cooling rate decreases rapidly, e.g. 0.07 K / Titan day at 70 km and 0.02 K / Titan day at 50 km, quite similar to Tomasko et al.'s results. On the other hand, we do not infer any decrease of this net radiative heating minus cooling above 120-130 km, but instead a regular increase up to 3 to 4 K per Titan day at 250-300 km. We note however that the decrease at higher altitudes invoked by Tomasko et al. is very uncertain given the large uncertainties in their haze model above 140 km, the altitude where the Huygens probe began measurements. Our haze model is also uncertain above ~200 km, where the net radiative heating minus cooling rate reaches ~2 K per Titan day.

We can also compare our calculations with the General Circulation Model (GCM) of Lebonnois et al. (2012, Fig. 10). At 20°S, their annual average of the solar heating rate is almost twice as large as ours at 90-100 km, 50% larger at 60 km and 30% larger at 50 km. These differences likely originate from differences in the haze model, that in Lebonnois et al.'s GCM being coupled with the 3-dimensional circulation and not imposed from observational constraints. More significant for our model comparison may be the ratio of dynamical cooling to total (radiative plus dynamical) cooling, also equal to radiative solar heating on an annual average basis. At 6°N, where seasonal modulation is minimum, this ratio can be determined from Fig. 10 of Lebonnois et al. at 85 and 66 km as approximately 18% and 25% respectively. Using the vertical velocity of 1.1 Pa / Titan day that we inferred in Section 4.3 at this latitude and the yearly-averaged solar heating rate from our model, we obtain ratios of 17% at 85 km and 28% at 66 km, in excellent agreement with Lebonnois et al.'s GCM outputs. Lebonnois et al. (2012) do not provide information to compare results above 100 km.

5.2 Radiative relaxation times

In Section 4.2, we calculated the radiative time constant (τ_R) corresponding to damping a temperature perturbation relative to the radiative equilibrium state, having a FWHM of one pressure scale height (Fig. 6). This time constant depends somewhat on the width of the temperature perturbation and doubling the width increases its value by 25% in the stratosphere. Strobel et al. (2009) provided another estimate of a radiative timescale by dividing temperature by the cooling rate, which actually corresponds to the time decay of temperature when the solar heating is turned off starting from the radiative equilibrium state. While this timescale may be appropriate to investigate diurnal variations of temperature, it strongly overestimates the time constant associated with the damping of small temperature perturbations around the radiative equilibrium state such as those caused by gravity waves or moderate seasonal variations of insolation. Figure 6 shows that our time constant τ_R is about a factor of 10 smaller than the timescale of Strobel et al., which is important to evaluate correctly the response of the atmosphere to e.g. seasonal forcing or planetary waves. For example, our calculation indicates that τ_R exceeds 1 Titan year only in the first 7 km of Titan's atmosphere while Strobel et al.'s estimation would predict that it happens at all altitudes below 76 km. In the upper troposphere and tropopause region, 30-60 km, τ_R is 0.25 to 0.3 Titan year, which allows for non-negligible seasonal variations of temperature in contrast to expectations using Strobel et al.'s simpler formulation. In the stratosphere, above 100 km ($p < 10$ mbar), τ_R is less than 0.03 Titan year (25 Titan days), so that significant seasonal temperature variations with almost no phase lag are expected.

As discussed by Flasar et al. (2014), the radiative time constant τ_R, as we define it here, can be formally written as $\left(\frac{\partial c(z)}{\partial T(z)}\right)^{-1}$ while Strobel et al. simply used $\left(\frac{c(z)}{T(z)}\right)^{-1}$. Using the cooling-to-space approximation and assuming that thermal cooling mostly occurs between the C_2H_2 band at 729 cm^{-1} and the CH_4 band at 1305 cm^{-1}, Flasar et al. estimated that the difference between the two estimations in the stratosphere could amount to a factor between 6 and 11, roughly in agreement with the factor of ~10 we find.

The cooling-to-space approximation was used by Achterberg et al. (2011) to estimate the radiative relaxation time at 5°S in the stratosphere. While their results are a factor of 2 to 3 smaller than $\frac{T(z)}{c(z)}$, they are still 4-5 times larger than our τ_R (Fig. 6). Achterberg et al. only considered opacity from C_2H_6, C_2H_2 and CH_4 and, based on Tomasko et al.'s (2008b) calculations, we estimate that the omission of other gases, and more importantly of haze, could explain a factor of 2 difference with our τ_R. The rest is at least partly due to the use of the cooling-to-space approximation which differs from our calculations where the perturbed layer, only one scale height thick, can also significantly cool by emitting to other atmospheric layers in addition to space.

5.3 Energy balance and adiabatic cooling

Comparing the radiative heating and cooling rates at 20°S in March 2007 (Section 4.1), we found that the former exceeds the latter by 20-35% in the range 0.1-5 mbar. Given that the actual temperature variation is at least an order of magnitude smaller than the radiative cooling rate, conservation of energy implies an additional source of cooling to balance the heating. The vertical upward velocity required to produce this cooling is about 0.09 cm s^{-1} at 1 mbar and varies approximately as $(\rho g)^{-1}$ from 1 to 5 mbar and as $(\rho g)^{-0.45}$ from 1 to 0.1 mbar.

Similarly, around 6°N, a latitude least sensitive to seasonal effects, the radiative heating exceeds the radiative cooling around equinox at all altitudes. As a result, the radiative solution for the temperature profile is warmer than the observed one at all levels (Section 4.3, Fig. 7). An exception is the region around 85-90 km, where the two profiles exhibit the same temperature with equal heating and cooling rates. This is due to the presence of the nitrile haze parametrized by Anderson and Samuelson (2011) which increases the cooling rate by ~30% at this altitude. The radiative equilibrium solution without this nitrile haze would be about 4 K warmer at 85-90 km where it peaks according to Anderson and Samuelson. Above 200 km, the uncertainty in the model temperature profile due the haze profile increases with height (Fig. 7). The difference between models using the lower and upper limits we fixed on the haze profile (Fig. 2) reaches ~3 K at 250 km (0.25 mbar), ~7 K at 300 km (0.09 mbar), ~13 K at 350 km (0.035 mbar) and ~15 K at 400 km (0.013 mbar). The coldest profile corresponds to the model of Doose et al. (2016) which has less aerosol density than the two other models. In fact, aerosol opacity provides both atmospheric cooling at long wavelengths and heating in the UV to near-infrared range, but the contribution to the heating dominates over that to the cooling.

To bring the model in general agreement with the Cassini/Huygens-derived profile at 6°N, we used an upward velocity profile w having 0.04 cm s^{-1} at 1 mbar, varying as $(\rho g)^{-1}$ below the 0.6-mbar level down to the troposphere, and as $(\rho g)^{-0.92}$ between 0.6 and 0.02 mbar (for our nominal haze model). The largest discrepancy takes place at altitudes of Anderson and Samuelson's (2011) nitrile haze (85-90 km, ~15 mbar) where the model is ~5 K colder than measured by Huygens/HASI at 10°S in 2005. This velocity profile corresponds to ~ -1 to -1.5 Pa per Titan day below the 0.02-mbar level (375 km), implying, from conservation of mass, no strong divergence of the vertical flux, i.e. weak variations of the latitudinal flow (black lines in Fig. 9). On the other hand, above the 0.02-mbar level, the vertical mass flux in this model is no longer approximately conserved and diverges horizontally in latitude. Note however that the velocity profile above ~220 km (0.5 mbar) is relatively uncertain due to uncertainties in the haze opacity profile. Using our lower limit for the haze density profile a significant divergence of the vertical mass flow is needed at much lower levels, ~1 mbar (Fig. 9). Also, although the nominal velocity profile allows us to reproduce generally well the temperature profile retrieved at 6°N, discrepancies of a few degrees remain in places. For example, the temperature gradient in the model from 1 to 0.1 mbar is not steep enough.

To fit more precisely the CIRS-derived temperatures from 4 to 0.2 mbar (Fig.14), we used a slightly different vertical variation of the velocity profile with a maximum, expressed in pressure units, at 0.4-1 mbar (185-225 km), decreasing above and, more slowly, below this pressure range (thin and dashed lines in Fig. 11). This would imply (weak) convergence of the vertical flow below this region, and divergence above, a feature generally consistent with the upwelling branch of a Hadley cell (e.g. Lora et al. 2015). The two velocity profiles, derived from fitting of the 6°N profile retrieved by Vinatier et al. (2015) and of the CIRS temperature maps at selected levels (Fig. 15), differ by at most 40% in the 4-0.2 mbar pressure range (at 1 mbar, 0.040 cm s^{-1} vs. 0.055 cm s^{-1}). This difference lies in the uncertainty area indicated in Fig. 9 and results from small systematic differences (typically 1-3 K) in the retrievals from Achterberg et al. (in preparation) and Vinatier et al. (2015). These differences partly result from the use of different sets of spectra (respectively nadir spectra at 2.8-cm^{-1} resolution and a combination of nadir and limb spectra at 0.5-cm^{-1} resolution) and the different vertical resolution of the retrievals.

5.4 Seasonal variations of temperatures from 0.2 to 4 mbar

At equatorial latitudes, we found that the modulation of solar heating due to Saturn's orbital eccentricity is large enough to explain the ~4 K drop between pre-equinox (2006-2008) and mid-2016 temperature at 1 mbar. The Sun-Saturn distance increased from 9.2 to 10.0 AU between January 2007 and January 2017, causing a decrease in insolation of 17%. This induces radiatively a ~7 K drop in the 1-mbar temperature (Fig. 10). To reduce this drop to the observed variation, a modulation of the adiabatic cooling is needed, with less cooling after equinox than before. Assuming for simplicity a sin(L_s) variation for this modulation, the upward velocity at 1 mbar in our best fit model varies between 0.035 and 0.075 cm s^{-1} over a Titan year.

At 30°S and 30°N, we also find that our radiative model with no modulation of the adiabatic cooling considerably overestimates the observed seasonal variation at all pressure levels between 0.2 and 4 mbar. Assuming that the vertical velocity at a given level is an affine function of sin(L_s) (Eq. 8) and that its vertical variation is the same at all latitudes, the observed variations of temperature are relatively well reproduced with the parameters listed in Table 1. An exception is the 4-mbar temperatures at the equator and 30°N, which show a steady decrease with time since the beginning of the Cassini mission. Such a variation cannot be reproduced with our simple radiative-dynamical model and would require a functional form for the time variation of the vertical velocity more complex than assumed in Eq. 8.

Our model shows that the time variation of the adiabatic cooling acts to counterbalance the seasonal variations of solar heating, with enhanced upwelling in summer. The modulation is stronger at 30°S than at 30°N, likely because the seasonal variations of solar heating are more pronounced in the southern hemisphere than in the northern one due to the eccentricity of Saturn's orbit, perihelion occurring less than a year after southern summer solstice. At the equator, the relatively weak modulation of the adiabatic cooling (~35%) acts to mitigate the variation of solar heating due to the eccentricity, with enhanced adiabatic cooling in northern winter / southern summer when the Sun-Saturn distance is smaller. At 30°N and more significantly at 30°S, our model predicts downwelling, and thus compressional heating, around winter solstice. At 30°S, the predicted maximum downward velocity at 0.5-1 mbar is 0.05 cm s^{-1}. This value is actually close to the downward velocity of 0.06 cm s^{-1} at 1 mbar required to balance the radiative cooling of 0.06 K day^{-1} derived by Teanby et al. (2017) near 80°S in January 2016. This would imply that, around winter solstice, subsidence is not limited to winter polar latitudes but extends equatorward to at least ~30°. Conversely, around equinox, for L_s between approximately 320° and 30°, upwelling occurs over the whole latitude range 30°S-30°N.

6. Conclusions

We have developed a one-dimensional seasonal radiative-dynamical model of Titan's atmosphere to investigate the temporal variations of Titan's stratospheric temperatures observed from 2004 to 2016 by Cassini/CIRS. This model calculates the radiative forcing using gas and haze vertical opacity profiles constrained by Cassini/CIRS and Huygens/DISR measurements. Adiabatic heating and cooling can occur by introducing a vertical velocity (*w*) in the energy equation. Applying this model to low latitudes, we conclude that:

- The heating and cooling rate profiles we obtained at 20°S are in good agreement with those calculated by Tomasko et al. (2008b). While the heating and cooling rates both decrease by a factor of ~20 from 0.1 to 5 mbar, the heating rate constantly exceeds the cooling rate by 20-35% over this range. We find that the net radiative heating minus cooling rate steadily increase with height from the troposphere up to 250 km, in contrast with Tomasko et al. (2008b) who suggested a maximum near 120 km.

- The radiative time constant (τ_R) associated with the damping of a small temperature perturbation, one-scale height broad, is typically one order of magnitude shorter than that simply estimated by dividing the temperature by the cooling rate (Strobel et al. 2009). Our radiative time constant is also significantly shorter than that estimated by Achterberg et al. (2011) using the cooling-to-space approximation and neglecting aerosol emission. We find that τ_R exceeds 10^9 s (i.e. a Titan year) only in the first half scale height of Titan's atmosphere, contrary to previous estimations. Above the 5-mbar level, τ_R is so short, less than 0.02 Titan year, that the solar heating rate and radiative plus dynamical cooling rate are essentially balanced at any time.
- At 6°N around equinox, where seasonal variations should be at minimum, we find that, as at 20°S, the heating rate exceeds the cooling rate at all altitudes and the radiative solution profile is thus warmer than the observed one. Adding adiabatic cooling with an upward velocity of ~ -1 to -1.5 Pa / Titan day (in pressure units) up to 375 km (0.02 mbar), brings the model profile in general agreement with the observed one. The corresponding velocity w varies thus approximately as the inverse of the atmospheric density in this range, with w ~ 0.03-0.05 cm s^{-1} at 1 mbar (185 km) and reaching its maximum, of the order of 1 cm s^{-1}, around 0.01 mbar (415 km). Our model is however affected by uncertainties in the haze density profile above ~225 km.
- Variations of solar heating due to Saturn's orbit eccentricity are more than sufficient to cause the decrease of equatorial temperatures observed from pre-equinox to 2016. A weak seasonal modulation of w (~35%) is needed to bring the radiative model variation (~7 K at 1 mbar) near the observed one (~4 K at 1 mbar). This modulation reduces the adiabatic cooling during northern summer, i.e. when the Sun-Saturn distance is larger, and enhances it during southern summer.

- The seasonal variations predicted by the radiative model with constant-with-time adiabatic cooling are also much larger than observed at 30°S and 30°N. A simple modulation of the vertical velocity profile as an affine function of sin(L_s) is capable of correctly reproducing the observed variations. While the required year-averaged velocity is upward (providing adiabatic cooling) at 0, 30°S and 30°N, subsidence is predicted to occur around winter solstice at 30°S and marginally at 30°N. At 1 mbar, w varies in the range 0.035–0.075 cm s^{-1} at the equator, -0.05 –0.16 cm s^{-1} at 30°S and -0.01–0.14 cm s^{-1} at 30°N along a Titan year.

These results may serve as a guide to general Circulation Models of Titan, which generally incorporate a less precise treatment of the radiative forcing. Although our radiative cooling and heating profiles are constrained by Cassini/Huygens observations, they still suffer from uncertainties in the haze opacity profile in the upper stratosphere and mesosphere. In particular, we have not considered variations with season of the haze profile at low latitudes, such as the evolution of the detached haze layer. We have also neglected the small seasonal variations of gaseous composition that may occur at 30°N or S. Nevertheless, the information given here should provide the basic radiative forcing at low latitudes for dynamical models.

We plan to extend this analysis to high latitudes where strong seasonal variations of composition and temperature are observed (e.g. Teanby et al. 2012, Vinatier et al. 2015, Coustenis et al. 2016, Teanby et al. 2017). The strong enhancement of photochemical species that takes place in the stratosphere during winter strongly affects the cooling rate profile and thus potentially the temperature profile. They clearly must be taken into account to characterize the adiabatic heating needed to balance the net radiative cooling, especially during the polar night.

Acknowledgments

BB and SV acknowledge support from the Centre National d'Études Spatiales (CNES) and the Programme National de Planétologie (INSU/CNRS). RKA was supported by the NASA Cassini Project. We thank the two referees whose thorough reviews helped to improve the paper.

References

Achterberg, R. K., Conrath, B. J., Gierasch, P. J., Flasar, F. M., Nixon, C. A., 2008a. Titan's middle-atmospheric temperatures and dynamics observed by the Cassini Composite Infrared Spectrometer. Icarus 194, 263-277. doi: 10.1016/j.icarus.2007.09.029.

Achterberg, R. K., Conrath, B. J., Gierasch, P. J., Flasar, F. M., Nixon, C. A., 2008b. Observation of a tilt of Titan's middle-atmospheric superrotation. Icarus 197, 549-555. doi: 10.1016/j.icarus.2008.05.014.

Achterberg, R. K., Gierasch, P. J., Conrath, B. J., Flasar, F. M., Nixon, C. A., 2011. Temporal variations of Titan's middle-atmospheric temperatures from 2004 to 2009 observed by Cassini/CIRS. Icarus 211, 686-698. doi: 10.1016/j.icarus.2010.08.009.

Anderson, C. M., Samuelson, R. E., 2011. Titan's aerosol and stratospheric ice opacities between 18 and 500 μm: Vertical and spectral characteristics from Cassini CIRS. Icarus 212, 762-768. doi: 10.1016/j.icarus.2011.01.024.

Bézard, B., Coustenis, A., McKay, C. P., 1995. Titan's stratospheric temperature asymmetry: A radiative origin? Icarus 113, 267-276. doi: 10.1006/icar.1995.1023.

Bézard, B., Nixon, C. A., Kleiner, I., Jennings, D. E., 2007. Detection of $^{13}CH_3D$ on Titan. Icarus 191, 397-400. doi: 10.1016/j.icarus.2007.06.004.

Coustenis, A., et al., 2013. Evolution of the stratospheric temperature and chemical composition over one Titanian year. Astrophys. J. 779, id. 177, 9 pp. doi: 10.1088/0004-637X/779/2/177.

Coustenis, A., et al., 2016. Titan's temporal evolution in stratospheric trace gases near the poles. Icarus 270, 409-420. doi: 10.1016/j.icarus.2015.08.027.

De Kok, R., et al., 2007. Oxygen compounds in Titan's stratosphere as observed by Cassini CIRS. Icarus 186, 354-363. doi: 10.1016/j.icarus.2006.09.016.

Doose, L. R., Karkoschka, E., Tomasko, M. G., Anderson, C. M., 2016. Vertical structure and optical properties of Titan's aerosols from radiance measurements made inside and outside the atmosphere. Icarus 270, 355-375. doi: 10.1016/j.icarus.2015.09.039.

Flasar, F. M., Conrath, B. J. 1990. Titan's stratospheric temperatures: A case for dynamical inertia? Icarus 85, 346-354. doi: 10.1016/0019-1035(90)90122-P.

Flasar, F. M., et al., 2004. Exploring the Saturn system in the thermal infrared: The Composite Infrared Spectrometer. Space Sci. Rev. 115, 169–297. doi: 10.1007/s11214-004-1454-9.

Flasar, F. M., Achterberg, R. K., Schinder, P. J., 2014. Thermal structure of Titan's troposphere and middle atmosphere. In: Müller-Wodarg, I., Griffith, C. A., Lellouch, E., Cravens, T. E. (Eds.), Titan – Interior, Surface, Atmosphere and Space Environment. Cambridge University Press, New York NY, pp. 102–121 (Chapter 3).

Fulchignoni, M., et al., 2005. In situ measurements of the physical characteristics of Titan's environment. Nature 438, 785-791. doi: 10.1038/nature04314.

Hirtzig, M., et al., 2013. Titan's surface and atmosphere from Cassini/VIMS data with updated methane opacity. Icarus 226, 470-486. doi: 10.1016/j.icarus.2013.05.033. Corrigendum: Icarus 226, 1182. doi: 10.1016/j.icarus.2013.07.015.

Irwin, P. G. J., Calcutt, S. B., Taylor, F. W., Weir, A. L., 1996. Calculated *k* distribution coefficients for hydrogen- and self-broadened methane in the range 2000-9500 cm^{-1} from exponential sum fitting to band-modelled spectra. J. Geophys. Res. 101, E11, 26137-26154. doi: 10.1029/96JE02707.

Jacquemart, D., et al., 2008. New laboratory measurements of CH_4 in Titan's conditions and a reanalysis of the DISR near-surface spectra at the Huygens landing site. Planet. Space Sci. 56, 613-623. doi: 10.1016/j.pss.2007.10.008.

Jacquinet-Husson, N., et al., 2011. The 2009 edition of the GEISA spectroscopic database. J. Quant. Spectrosc. Radiat. Trans. 112, 2395-2445. doi: 10.1016/j.jqsrt.2011.06.004.

Karkoschka, E., Lorenz, R. D., 1997. Latitudinal variation of aerosol sizes inferred from Titan's shadow. Icarus 125, 369-379. doi: 10.1006/icar.1996.5621.

Karkoschka, E., Tomasko, M. G., 2010. Methane absorption coefficients for the jovian planets from laboratory, Huygens, and HST data. Icarus 205, 674-694. doi: 10.1016/j.icarus.2009.07.044.

Karkoschka, E., Schröder, S. E., Tomasko, M. G., Keller, H. U., 2012. The reflectivity spectrum and opposition effect of Titan's surface observed by Huygens' DISR spectrometers. Planet. Space Sci. 60, 342-355. doi: 10.1016/j.pss.2011.10.014.

Landau, L., Lifchitz, E., 1969. Physique théorique. Tome I. Mécanique. 3rd edition (revised). Ed. MIR, Moscow.

Lebonnois, S., Burgalat, J., Rannou, P., Charnay, B., 2012. Titan global climate model: A new 3-dimensional version of the IPSL Titan GCM. Icarus 218, 707-722. doi: 10.1016/j.icarus.2011.11.032.

Lebonnois, S., Flasar, F. M., Tokano, T., Newman, C. E., 2014. The general circulation of Titan's lower and middle atmosphere. In: Müller-Wodarg, I., Griffith, C. A., Lellouch, E., Cravens, T. E. (Eds.), Titan – Interior, Surface, Atmosphere and Space Environment. Cambridge University Press, New York NY, pp. 122–157 (Chapter 4).

Lellouch, E., et al., 2014. The distribution of methane in Titan's stratosphere from Cassini/CIRS observations. Icarus 231, 323-337. doi: 10.1016/j.icarus.2013.12.016.

Lora, J. M., Lunine, J. I., Russell, J. L. 2015. GCM simulations of Titan's middle and lower atmosphere and comparison to observations. Icarus 250, 516-528. doi: 10.1016/j.icarus.2014.12.030.

Newman, C. E., Lee, C., Lian, Y., Richardson, M. I., Toigo, A. D., 2011. Stratospheric superrotation in the TitanWRF model. Icarus 213, 636-654. doi: 10.1016/j.icarus.2011.03.025.

Niemann, H. B., et al., 2010. Composition of Titan's lower atmosphere and simple surface volatiles as measured by the Cassini-Huygens probe gas chromatograph mass spectrometer experiment. J. Geophys. Res. 115, E12006. doi: 10.1029/2010JE003659.

Press, W. H., Teukolsky, S. A., Vetterling, W. T., Flannery, B. P., 1997. *Numerical Recipes in Fortran 77: The Art of Scientific Computing* (Vol. 1 of Fortran Numerical Recipes). Cambridge Univ. Press, New York NY (Chapter 15).

Rey, M., Nikitin, A. V., Bézard, B., Rannou, P., Coustenis, A., Tyuterev, V. G., 2017. New accurate theoretical line lists of $^{12}CH_4$ and $^{13}CH_4$ in the 0-13400 cm^{-1} range: Application to the modelling of methane absorption in Titan's atmosphere. Icarus, submitted.

Rothman, L. S., et al., 2013. The HITRAN2012 molecular spectroscopic database. J. Quant. Spectrosc. Radiat. Trans. 130, 4-50. doi: 10.1016/j.jqsrt.2013.07.002.

Stamnes, K., Tsay, S-C., Wiscombe, W., Jayaweera, K., 1988. Numerically stable algorithm for discrete-ordinate-method radiative transfer in multiple scattering and emitting layered media. Appl. Opt. 27, 2502-2509. doi: 10.1364/AO.27.002502.

Strobel, D. F., et al., 2009. Atmospheric structure and composition. In: Brown, R. H., Lebreton, J.-P., Waite, J. H. (Eds.), Titan from Cassini-Huygens. Springer, Dordrecht, pp. 235–257 (Chapter 10).

Teanby, N. A., et al., 2007. Vertical profiles of HCN, HC_3N, and C_2H_2 in Titan’s atmosphere derived from Cassini/CIRS data. Icarus 186, 364-384. doi: 10.1016/j.icarus.2006.09.024.

Teanby, N. A., et al., 2008. Global and temporal variations in hydrocarbons and nitriles in Titan's stratosphere for northern winter observed by Cassini/CIRS. Icarus 193, 595-611. doi: 10.1016/j.icarus.2007.08.017.

Teanby, N. A., Irwin, P. G. J., de Kok, R., Nixon, C. A. 2009. Dynamical implications of seasonal and spatial variations in Titan’s stratospheric composition. Phil. Trans. Royal Soc. 367, 697-711. doi: 10.1098/rsta.2008.0164.

Teanby, N. A., et al., 2012. Active upper-atmosphere chemistry and dynamics from polar circulation reversal on Titan. Nature 491, 732-735. doi: 10.1038/nature11611.

Teanby, N. A., et al., 2017. The formation and evolution of Titan’s winter polar vortex. Nat. Commun., in press.

Tomasko, M. G., Bézard, B., Doose, L., Engel, S., Karkoschka, E., 2008a. Measurements of methane absorption by the descent imager/spectral radiometer (DISR) during its descent through Titan’s atmosphere. Planet. Space Sci. 56, 624-647. doi: 10.1016/j.pss.2007.10.009.

Tomasko, M. G., Bézard, B., Doose, L., Engel, S., Karkoschka, E., Vinatier, S., 2008b. Heat balance in Titan's atmosphere. Planet. Space Sci. 56, 648-659. doi: 10.1016/j.pss.2007.10.012.

Tomasko, M. G., et al., 2008c. A model of Titan's aerosols based on measurements made inside the atmosphere. Planet. Space Sci. 56, 669-707. doi: 10.1016/j.pss.2007.11.019.

Vinatier, S., et al., 2007. Vertical abundance profiles of hydrocarbons in Titan's atmosphere at 15° S and 80° N retrieved from Cassini/CIRS spectra. Icarus 188, 120-138. doi: 10.1016/j.icarus.2006.10.031.

Vinatier, S., et al., 2010a. Analysis of Cassini/CIRS limb spectra of Titan acquired during the nominal mission. I. Hydrocarbons, nitriles and CO_2 vertical mixing ratio profiles. Icarus 205, 559-570. doi: 10.1016/j.icarus.2009.08.013.

Vinatier, S., et al., 2010b. Analysis of Cassini/CIRS limb spectra of Titan acquired during the nominal mission. II: Aerosol extinction profiles in the 600-1420 cm^{-1} spectral range. Icarus 210, 852-866. doi: 10.1016/j.icarus.2010.06.024.

Vinatier, S., Rannou, P., Anderson, C. A., Bézard, B., de Kok, R., Samuelson, R. E., 2012. Optical constants of Titan's stratospheric aerosols in the 70-1500 cm^{-1} spectral range constrained by Cassini/CIRS observations. Icarus 219, 5-12. doi: 10.1016/j.icarus.2012.02.009.

Vinatier, S., et al., 2015. Seasonal variations in Titan's middle atmosphere during the northern spring derived from Cassini/CIRS observations. Icarus 250, 95-115. doi: 10.1016/j.icarus.2014.11.019.

Vinatier, S., et al., 2016. Seasonal variations in Titan's stratosphere observed with Cassini/CIRS after the northern spring equinox. American Astronomical Society, DPS meeting #48, id.509.09.

Vinatier, S., et al., 2017a. Study of Titan's fall southern stratospheric polar cloud composition with Cassini/CIRS: detection of benzene ice. Icarus, submitted.

Vinatier, S., et al., 2017b. Seasonal variations in Titan's stratosphere observed with Cassini/CIRS during northern spring. American Astronomical Society, DPS meeting #49, id.304.03.